Supporting Information: The impact of C_{60}-self-assembled monolayer electron-transport layers in negative-intrinsic-positive perovskite solar cells

Suer Zhou [a], Luca Gregori [b,c], Seongrok Seo [a], Raghunath R. Dasari [d], Jae Eun Lee [a], Edoardo Mosconi [b], Heon Jin [a], Francesca Nunzi [b,c], Fengning Yang [a], Manuel Kober-Czerny [a], Alexandra J. Ramadan [a,e], Akash Dasgupta [a], Leonardo Pacifici [b], Igal Levine [f,g], Joel Smith [a], Stephen Barlow [d,h], Laura M. Herz [a], Filippo De Angelis[b,c,i], Seth R. Marder [d,h,j], Henry J. Snaith [a]*

[a] Department of Physics, University of Oxford, Clarendon Laboratory, Parks Road, Oxford, OX1 3PU, UK

[b]Computational Laboratory for Hybrid/Organic Photovoltaics (CLHYO), Istituto CNR di Scienze e Tecnologie Chimiche "Giulio Natta" (CNR-SCITEC), Via Elce di Sotto 8, 06123 Perugia, Italy

[c]Department of Chemistry, Biology and Biotechnology, University of Perugia, 06123, Italy

[d] School of Chemistry and Biochemistry and Center for Organic Photonics and Electronics, Georgia Institute of Technology**,** North Avenue, Atlanta, GA 30332, USA

[e] School of Mathematical and Physical Sciences, University of Sheffield, Hounsfield Road, Sheffield, S3 7RH, UK

[f] Division Solar Energy, Helmholtz-Zentrum Berlin für Materialien und Energie GmbH, Hahn-Meitner-Platz 1, 14109 Berlin, Germany

[g] Institute of Chemistry and The Center for Nanoscience and Nanotechnology, The Hebrew University of Jerusalem, Jerusalem 9190401, Israel

[h] Renewable and Sustainable Energy Institute, University of Colorado Boulder, 4001 Discovery Drive, Boulder, CO 80309, USA.

[i] SKKU Institute of Energy Science and Technology (SIEST), Sungkyunkwan University, Suwon 440-746, South Korea

[j] Department of Chemical and Biological Engineering, University of Colorado Boulder, 3415 Colorado Avenue, Boulder, CO 80309, USA and Department of Chemistry, University of Colorado Boulder, 1606 Central Campus Mall, Boulder, CO 80309, USA

*Corresponding author: henry.snaith@physics.ox.ac.uk

Experimental Methods

Materials

Tin (II) chloride dihydrate (99.995%), urea (≥98%), hydrochloric acid (37%), thioglycolic acid (≥99%), and 1-butyl-1-methylpiperidinium tetrafluoroborate ($[BMP]^+[BF4]^-$) (99%) were purchased from Sigma-Aldrich. Ultrapure water was purchased from Cambridge Bioscience. Formamidinium iodide (FAI) (99.999%) and methylammonium chloride (MACl) were purchased from Dyenamo. Methylammonium bromide (MABr) was purchased from Xi'an Polymer Light Technology Corp. Lead(II) iodide (PbI_2) (99.999%) was purchased from Alfa Aesar. Lead(II) bromide ($PbBr_2$) (>98.0%) was purchased from TCI. Phenethylammonium iodide (PEAI) and n-octylammonium bromide were purchased from GreatCell Solar Materials. 2,2′,7,7′-tetrakis(*N,N′*-di-p-methoxyphenylamino)-9,9′-spirobifluorene (Spiro-OMeTAD) (>99.5%) was obtained from Lumtech. Lithium bis(trifluoromethanesulfonyl)imide (Li-TFSI, >99%), 4-tert-butylpyridine (tBP, 98%), Isopropanol (IPA, 99.5%), N, N-dimethylformamide (DMF, anhydrous 99.8%), dimethyl sulfoxide (anhydrous DMSO, >99.9%), anisole (anhydrous, 99.7%), chlorobenzene (CB, 99.8%), acetonitrile (ACN, anhydrous 99.8%), tetrahydrofuran (≥99.9%), Al_2O_3 nanoparticles (20 wt.% in isopropanol) were purchased from Sigma-Aldrich. The 4-(1',5'-Dihydro-1'-methyl-2'H-[5,6]fullereno-C60-Ih-[1,9-c]-pyrrol-2'-yl)benzoic acid (C_{60}-CA) was used as purchased from Luminescence Technology Corp. Chemicals were used as received without further purification. Gold pellets and chromium bar for evaporation were purchased from Kurt J. Lesker.

Synthesis of C_{60}-PA.

The synthesis of 4-(1',5'-dihydro-1'-methyl-2'*H*-[5,6]fullereno-C60-I_h-[1,9-*c*]-pyrrol-2'-yl)phenylphosphonic acid (C_{60}-PA) was adapted from reference. [1] Specifically, the diethyl ester of C_{60}-PA was synthesized according to the literature, but in our hands the final hydrolysis step was unsuccessful following the conditions of reference 1, which reported the use of CH_2Cl_2 as the solvent and no heating; however, we were able to obtain good yields of the final acid using dichloroethane and heating as follows.

The diethyl ester of C_{60}-PA (0.20 g, 0.20 mmol) was dissolved in dry 1,2-dichloroethane (75 mL) at 75 °C. Bromotrimethylsilane (0.21 mL, 1.61 mmol, 8 eq.) was then added, and the mixture was heated at 75 °C for 14 h. Upon completion of the reaction, it was quenched by the addition of water (10 mL), and the volatiles were removed under reduced pressure. The resulting precipitate was filtered, washed with water and methanol, and dried under vacuum

to yield C_{60}-PA as a brown solid (0.18 g, 95%). The ^{1}H NMR spectrum and other characterization data are consistent with those reported in the literature.[1]

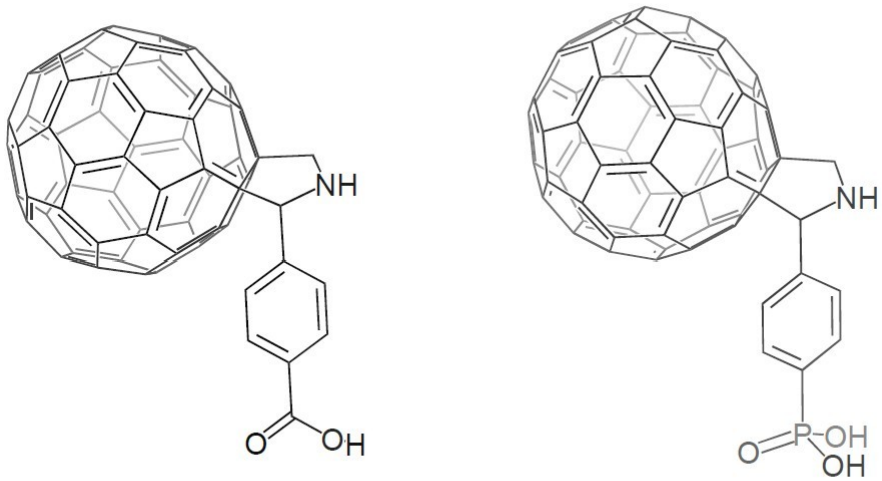

The structure of the C_{60}-CA SAM (left) and the structure of the C_{60}-PA SAM (right).

n-i-p Device Fabrication

Substrate Cleaning

Pre-etched FTO substrates (Pilkington Tec7) were cleaned by subsequently sonicating in Decon 90 solution (1% vol. in D.I. water), D.I. water, acetone, isopropanol for 10 min each. Then they were dried in a stream of nitrogen and UV-ozone cleaned for 15 min.

SnO_2 Chemical Bath Deposition

17.4 mg/ml tin (II) chloride dihydrate was dissolved in isopropanol and spin-coated onto the FTO substrates at 3,000 rpm for 25 s under ambient atmosphere. Subsequently, they were dried on a hotplate at 100 °C for 10 min. Then the hotplate temperature was increased to 180 °C and the substrates were annealed for 1 h and then they were cooled to room temperature. A chemical bath solution containing 200 mL D.I. water, 2.5g urea, 50 µL thioglycolic acid, 2.5 mL hydrochloric acid and 540 mg tin (II) chloride dihydrate was stirred until fully dissolved. The substrates were then laid inside a Pyrex glass dish with FTO side face up. The chemical bath solution was added into to the glass dish and closed with a glass lid. The container was left in a 90 °C oven for 3~4 h for the chemical bath deposition. Afterward, the

substrates were taken out and subsequently sonicated in D.I. water and isopropanol for 5 min each and dried with a nitrogen gun. Then the substrates were annealed again at 180 °C for 1 h. The substrates were further put under UV-ozone cleaning for 20 min before SAMs deposition.

C_{60}-PA Deposition

C_{60}-phosphonic acid was dissolved in DMSO at a concentration of 1 mM (0.932 mg/mL). Due to the low solubility of the SAM, the vial was first stirred at 70°C for 1 day and then sonicated at 40 °C for 3 h. The solution was subsequently passed through a 0.45 μm and then a 0.22 μm PTFE filter right before use. The SAM solution was dropped onto the substrate and spun at 3,500 rpm for 1 min and then annealed at 100 °C for 10 min. Afterward, any excess unbound C_{60}-phosphonic acid was rinsed away with pure DMSO solvent using the same spin coating program and dried again at 100 °C for 10 min.

C_{60}-CA Deposition

C_{60}-carboxylic acid was dissolved in a 1:1 v:v co-solvent of tetrahydrofuran: chlorobenzene (THF:CB) at a concentration of 1 mM. The solution was passed through a 0.22 μm PTFE filter right before use. The SAM solution was dropped onto the substrate and spun at 3,500 rpm for 1 min and then annealed at 100 °C for 10 min. Afterward, any excess unbound C_{60}-carboxylic acid was rinsed away with pure THF:CB solvent using the same spin coating program and dried again at 100 °C for 10 min.

Al_2O_3 Nanoparticles Deposition

500 μL of a 1:150 Al_2O_3 nanoparticles:isopropanol solution was statically spin-coated onto the substrates as a wetting layer at 5,000 rpm speed for 20 s with 5,000 rpm/sec acceleration and subsequently annealed at 100 °C for 2 min.

$FAPbI_3$ (with 35% MACl and 1% $MAPbBr_3$) Perovskite Deposition

1.5 M $FAPbI_3$ 99% with 35% excess MACl and 1% $MAPbBr_3$ additive was used as the absorber material and prepared in a nitrogen-purged glovebox. 255.4 mg of FAI, 35.4 mg of MACl, 1.7 mg of MABr, 684.6 mg PbI_2, and 5.5 mg of $PbBr_2$ were dissolved in 1 mL of 4:1 DMF:DMSO. The solution was stirred on the hotplate at room temperature for 1 h. The solution was passed through a 0.45 μm filter before use. Inside a condensed dry air purged drybox with around 10% relative humidity, 100 μL of precursor solution was drop-casted on

the substrate and spun at 6,000 rpm for 30 s (3000 rpm/s ramp speed). 300 µL of anisole was dripped onto the substrate 10 s into the spinning program. The perovskite films were dried at 80 °C until all substrates are spun and then annealed at 150 °C for 15 min.

$FA_{0.83}Cs_{0.17}Pb(I_{0.9}Br_{0.1})_3$ Perovskite Deposition

1.45 M $FA_{0.83}Cs_{0.17}Pb(I_{0.9}Br_{0.1})_3$ precursor solution was made by dissolving 64.0 mg CsI, 79.8 mg $PbBr_2$, 207.0 mg FAI, and 568.2 mg PbI_2, 0.2 mol% of $BMPBF_4$ (with respect to the Pb) into every 1 mL of a DMF:DMSO solvent mixture (4:1 volume ratio). The precursor solution was stirred on a hotplate at room temperature for 1 h in a nitrogen-purged glovebox before use. The solution was passed through a 0.45 µm PTFE filter and transferred to a condensed dry air-purged drybox at around 10% relative humidity for perovskite deposition. Then 70 µL of the precursor solution was spread on an FTO/SnO_2 substrate using a pipette tip and then spun at a spin speed of 6,000 rpm for 35 s (with a ramp speed of 2,000 rpm/s). 150 µL anisole was dropped at the center 10 s before the end of spinning. The film was annealed on a hotplate at 100 °C for 45 min.

PEAI Passivation on Perovskite

After the perovskite layer deposition, a 5 mM phenethylammonium iodide (PEAI) was dissolved in isopropanol and spin coated onto the perovskite layer for passivation. The PEAI solution was drop-casted onto the substrate dynamically spinning at 3,000 rpm for 30 s without annealing.

n-Octylammonium Bromide Passivation on Perovskite

For the devices tested for stability, a 5 mM n-octylammonium bromide (OABr) was dissolved in isopropanol and spin coated onto the perovskite layer for passivation. The OABr solution was drop-casted onto the substrate dynamically spinning at 5,000 rpm for 30 s and then annealed at 100°C for 10 min.

Spiro-OMeTAD Deposition

For the hole-transporting layer, 85 mg/ml Spiro-OMeTAD was dissolved in chlorobenzene. 33 µL of *tert*-butyl pyridine (tBP) was added to per 1mL of the Spiro-OMeTAD solution first. A 517 mg/ml Li-TFSI stock solution in acetonitrile was made separately. Then 20 µL of the Li-TFSI solution was added to per 1 mL of Spiro-OMeTAD solution. The Spiro-

OMeTAD solution was filtered with a 0.22 μm filter and dynamically dropped onto the substrate spinning at 2,500 rpm (2,500 rpm/s ramp) for 30 s.

PTAA Deposition

10 mg/ml PTAA was dissolved in toluene and stirred until fully dissolved. The solution was filtered through a 0.22 μm filter and then dynamically dropped onto the substrate spinning at 3,000 rpm (3,000 rpm/s ramp) for 30 s. The PTAA layer on perovskite is on average around 15 nm thick.

Metal Electrode Evaporation

For the top metal contact, the evaporation chamber was pumped down until the pressure reaches $<5 \times 10^{-6}$ Torr. Then 80 nm of Au was evaporated at the rate of 0.1 Å/s for the first 10 Å and then the evaporation rate was gradually increased to 0.7 Å/s for the rest. For Cr/Au evaporation, first, 3.5 nm Cr was evaporated at the rate of 0.1 Å/s then the same Au program was subsequently used to evaporate 80 nm of Au.

Half-stack ETL/Perovskite Samples Fabrication

The half-stack samples for the terahertz spectroscopy characterization were made on quartz substrates. Subsequently, the ETL and $FAPbI_3$ perovskite layers were fabricated following the same procedure as reported in the experimental methods. Afterward, a PMMA layer was processed on top of the perovskite film to encapsulate it. 20 mg/mL PMMA layer was spin coated on top of the half-stack at a spin speed of 2,000 rpm (2,000 rpm/s ramp rate) for 20 s.

Contact Angle Measurements

The contact angles of the C_{60}-SAMs films on FTO were measured using a video-based optical contact angle measuring device (Ossila Contact Angle Goniometer) and analyzed using the Ossila Contact Angle 3.0.9.1 software. All measurements were performed in ambient atmosphere and at room temperature.

UV-vis Absorption

Absorption spectra were measured in dilute solutions in a cuvette and on glass substrates using a UV/Vis-NIR spectrophotometer, Lambda 35 (Perkin-Elmer).

Time-Correlated Single Photon Counting

Steady-state and time-resolved PL measurements were acquired using a time-correlated single-photon counting (TCSPC) setup (FluoTime 300, PicoQuant GmbH). Film samples were photoexcited using a 405 nm laser head (LDH-P-C-405, Pico Quant GmbH) pulsed at a frequency of 300 kHz, with a pulse duration of 128 ps~4 ns. The PL was collected using a high-resolution monochromator and hybrid photomultiplier detector assembly (PMA Hybrid 40, PicoQuant GmbH) with a detection wavelength set to the peak PL emission wavelength from the sample.

The time-resolved PL decays were fitted to a stretched-exponential function

$$f(t) = A\, e^{-\left(\frac{t}{\tau}\right)^{\beta}} \qquad \textbf{Equation S1}$$

in which β is the stretching parameter. 0<β<1 indicates how much the curve deviates from a mono-exponential decay of β=1. The mean lifetime of the photogenerated charges ⟨τ⟩ is given by

$$¿\tau \geq \int_0^{\infty} e^{(-(\frac{t}{\tau})¿¿\beta)dt} ¿= \frac{\tau}{\beta}\Gamma\left(\frac{1}{\beta}\right) \qquad \textbf{Equation S2}$$

where Γ is the gamma function. The fitting method is detailed in this paper published by Habisreutinger et al.[2]

Photoluminescence Quantum Yield

PLQY values were determined following the method of De Mello et. al.[3] using a 532 nm continuous wave laser excitation source (Roithner, RLTMLL-532 2 W) to illuminate a sample in an integrating sphere (Newport, 70682NS), and the laser scatter and PL were collected using a fiber-coupled spectrometer (Ocean Optics MayaPro). The beam intensity was modified using neutral density filters. To obtain PLQY values that correlate with a

device operating under 1 sun illumination for a particular wavelength laser, an optical density filter was used to adjust the laser output to the equivalent of AM 1.5G for each perovskite bandgap. See Figure 3 from Kirchartz et al.[4]

Optical-Pump Terahertz-Probe Measurements

Our Optical-pump Terahertz-probe (OPTP) setup (described in more detail in reference [5,6]) uses a Spectra Physics Mai Tai-Ascend-Spitfire Pro Ti:Sapphire regenerative amplifier. The amplifier generates an ultra-fast laser with 35 fs pulse duration, 800 nm centre wavelength and 5 kHz repetition rate. 400 nm optical pump excitation wavelength was achieved by frequency doubling the fundamental laser output through a BBO crystal. THz probe pulses were generated with by a spintronic emitter which consists of quartz/2 nm Tungsten/1.8 nm $Co_{40}Fe_{40}Be_{20}$/2 nm Platinum. The sample stored in an evacuated chamber at pressure less than 10^{-1} mbar was excited with the pump and probed with the THz pulse shortly after. The pump and THz pulses were chopped with optical choppers with frequencies of 1.25 and 2.5 kHz respectively to obtain the THz transmission change ΔT. The sigma spread (σ) of pump and probe beam at the sample positions were measured as 2.1 mm and 0.3 mm respectively. For a Gaussian beam, FWHM and sigma are related as $FWHM = 2\sigma\sqrt{2\ln 2}$. The power of pump pulses was tuned by a ND filter wheel. The THz transmission from samples was detected by electro-optic sampling in a (110)-ZnTe crystal (1 mm thickness) with a spatially and temporally overlapping 800 nm gate pulse. The THz transmission was measured at the peak of the THz pulse for different delays of the pump beam, mapping the THz transmission as a function of time after photoexcitation. The OPTP decay traces with different delays were measured for 4 fluences on the substrate side for each sample. The identical experimental procedure was repeated after each aging time.

Charge-Carrier Mobility from Change in THz Electric Field Transmission

The effective charge-carrier mobility was extracted from the OPTP data using the method illustrated previously by Wehrenfennig *et al* [6]. The sheet photoconductivity ΔS of a thin film between two media of refractive indices n_A and n_B with its thickness much smaller than the THz wavelength can be expressed as:

$$\Delta S = -\epsilon_0 c (n_A + n_B) \left(\frac{\Delta T}{T} \right) \qquad \textbf{Equation S3}$$

where ϵ_0 is the vacuum permittivity, c is the speed of light and $\Delta T/T$ is the ratio of photo-induced change in the THz electric field to the transmitted THz electric field in the dark. In this study, n_A is the refractive index of a z-cut quartz, which is 2.13 and n_B is the refractive index of vacuum which is 1.

Deriving the charge-carrier mobility μ from ΔS requires the knowledge of the number of photo-excited charge-carriers N, which can be calculated as:

$$N = \varphi \frac{E\lambda}{hc} \left(1 - R_{pump} - T_{pump}\right) \qquad \textbf{Equation S4}$$

where φ is the photon-to-charge branching ratio, E is the energy obtained in an optical excitation pulse with wavelength λ, h is the Planck's constant, R_{pump} and T_{pump} are the reflected and transmitted fractions of the pump beam. Then, μ can be calculated with:

$$\mu = \frac{\Delta S A_{eff}}{Ne} \qquad \textbf{Equation S5}$$

where A_{eff} is the effective area of the overlap of optical pump and THz probe pulse considering the Gaussian beam profiles and e is the elementary charge. As reported by Xia et al.,[7] A_{eff} is defined as $A_{eff} = 2\pi \left({\sigma_{pump}}^2 + {\sigma_{THz}}^2 \right)$, where σ_{pump} and σ_{THz} are the pump and THz beam waists, respectively. To avoid artifacts, the ratio between σ_{pump} and σ_{THz} is fixed at ~6.[8] By using the above equations, the effective mobility $\tilde{\mu} = \varphi\mu$ is expressed as:

$$\varphi\mu = -\epsilon_0 c (n_A + n_B) \frac{A_{eff} hc}{E\lambda e \left(1 - R_{pump} - T_{pump}\right)} \left(\frac{\Delta T}{T} \right) \qquad \textbf{Equation S6}$$

In this work, we assume $\varphi = 1$ given that the exciton binding energies are low and free charge-carriers are dominant right after excitation.[9,10] The charge-carrier mobility obtained here is the sum of electron and hole mobilities and they cannot be separated.

To obtain $\varphi\mu$, $\Delta T/T$ at time zero against E was plotted and a linear function was fitted based on **Equation S6** up to the point where nonlinear processes were not observed. Then, $\varphi\mu$ was obtained from the gradient.

Fast-Hysteresis Measurement

In order to assess the transient ionic current loss occurring in our devices, an in-house built fast J-V setup was used.

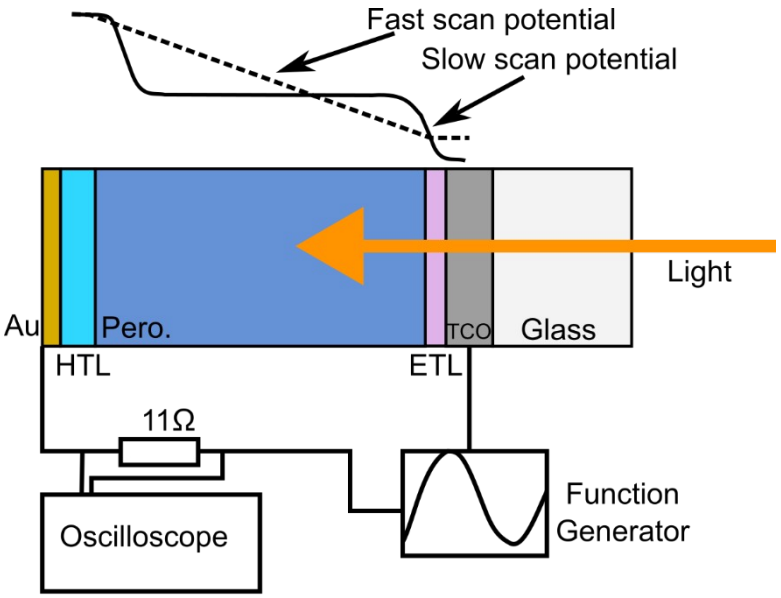

Schematic illustration of the 'Fast-Hysteresis' measurement setup.

The device was connected to a function generator (RSDG 1032X) coupled to a generic operational amplifier, with a 11 Ω resistor placed in series. The forward and reverse voltage sweep is induced by sending a triangular pulse at a set frequency to the device, with the amplifier providing the power to drive the cell. The current is measured by measuring the potential drop across the resistor in series and converting this to a current through ohms law. This is done using a digitizer (Picoscope 204A), giving us a current-to-time trace. A trigger pulse from the function generator is coupled into the digitizer, allowing time synchronization, allowing us to link the trace time to the applied voltage to infer the J-V curve. These J-V curves were measured over a large range of frequency in logarithmically spaced intervals,

allowing us to estimate the device performance as the scan speeds move past the timescale of the ionic current in the active layer. Due to significant noise, 10 repeats for each applied frequency were taken and averaged, and a spline fit was performed for the extracted parameters (V_{oc}, J_{sc}, *FF*, *MPP*).

Time-resolved Surface Photovoltage (tr-SPV)

Low frequency tr-SPV measurements were performed in an N_2 environment using a 620 nm excitation laser light from a diode pumped tunable pulse laser (Nd:YAG, EKSPLA, NT230-50, duration time of laser pulses 3 – 5 ns) with a spectral cleaning unit. The measurement frequency was 2 Hz, 100 averages were taken per transient, and the laser intensity was controlled using neutral density filters. The SPV transients were measured with an oscilloscope card (Gage, CSE 1622- 4GS, 200 MS/s) using an in-house developed software for logarithmic read-out.[11] For more details and a schematic of the tr-SPV setup see ref. [12]

Grazing-incidence wide-angle X-ray scattering (GIWAXS)

The GIWAXS data were recorded with a Rigaku SmartLab diffractometer, equipped with a HyPix-3000 hybrid pixel-array 2D detector and a rotating 3 kW Cu Kα source (operating at 40 kV, 45 mA). X-ray photons with energy of 8.048 keV and CBO-f optics were incident on an aligned sample surface, held at grazing incidence angles of 1 ° and 2°. The samples were mounted on a 2D-XRD attachment stage with a beam stop for the direct beam, which was positioned 65 mm away from the detector. Detector images were integrated and resampled into Q-space and were combined using scripts based on the PyFAI and pygix libraries. These libraries were also used for azimuthally integrated 1D profiles. For variable-angle GIWAXS measurements (αi = 1°−2°), samples were measured using a different 2D-XRD aperture slit configuration with parallel-beam optics, a 0.5° in-plane parallel-slit collimator, a 0.1 mm incident slit, and a 10 mm length-limiting slit at a single detector position, before processing as described above.

To calculate the X-ray attenuation length, we use the following equation[13]:

$$L_{atten} = \frac{1}{\mu'} = \frac{cos\theta}{(\mu/\rho)\rho}$$

where L_{atten} is the attenuation length, μ' is the effective linear attenuation coefficient, μ is the linear attenuation coefficient, (μ/ρ) is the mass attenuation coefficient, and ρ is the density of the material, θ is the grazing incidence angle. The mass attenuation coefficient depends on the X-ray energy and the chemical composition of the material. The density of the material is calculated based on the composition of $FAPbI_3$. At grazing incidence angles of 1°, 1.5° and 2°, the attenuation lengths are calculated to be 161.01 nm, 250 nm and 335 nm, respectively.

X-ray Photoelectron Spectroscopy (XPS) and Ultraviolet Photoelectron Spectroscopy (UPS)

The x-ray photoelectron spectroscopy (XPS) data were collected at the Photoemission Research Technology Platform, University of Warwick. The samples investigated in this study were attached to electrically-conductive carbon tape and mounted on to a sample bar, before being loaded into a Kratos Axis Ultra DLD spectrometer which possesses a base pressure below 1×10^{-10} mbar. XPS and UPS measurements were performed in the main analysis chamber at room temperature and at a take-off angle of 90° with respect to the surface parallel. The work function and binding energy scale of the spectrometer were calibrated using the Fermi edge and $3d_{5/2}$ peak recorded from a polycrystalline Ag sample prior to the commencement of the experiments. UPS measurements were performed using a UV light source and He Iα emission (hν = 21.22 eV), using an analysis area of 110 microns in diameter and an analyzer pass energy of 5 eV (resolution approx. 0.1 eV). Data were analyzed in the CasaXPS package using the edge up and edge down functions to extrapolate the secondary electron cutoff and valence band maximum to the background intensity. For XPS, the samples were illuminated by a monochromated Al Kα x-ray source (hν = 1486.7 eV). The core level spectra were recorded using a pass energy of 20 eV (resolution approx. 0.4 eV), from an analysis area of 300×700 μm^2. The data were analyzed in the CasaXPS package using Shirley backgrounds and mixed Gaussian-Lorentzian (Voigt) lineshapes, with asymmetry parameters where appropriate. For compositional analysis, the analyzer transmission function has been determined using clean metallic foils to determine the detection efficiency across the full binding energy range.

Density Functional Theory Calculations

To model the interaction between the substituted fullerene molecules and the SnO_2 surface we constructed model slabs of the (110) surface. We used a 2 × 2 supercell, with a and b parameters of 12.75 and 13.40 Å, respectively. 25 Å vacuum were left along the z direction.

Calculations were carried out by the Quantum Espresso package,[14,15] employing the Perdew-Burke-Ernzenhof (PBE) exchange correlation functional[16] together with Grimme D3[17] corrections. Electron-ion interactions were described by norm conserving pseudopotentials from the PseudoDojo repository[18] with electron from 5s, 5p; N, C 2s, 2p; O 2s 2p; H 1s; Sn 6s, 6p, 5d shells explicitly included in the calculations. Plane wave cut-offs for the smooth part of the wavefunctions and the augmented density were 60 and 240 Ry respectively. Hybrid PBE0[19] calculations on the unit cell of bulk SnO_2 have been carried out using relativistic norm-conserving pseudopotentials without linear core-correction (shells explicitly included in calculations: I 5s, 5p; N, C 2s, 2p; H 1s; Sn 5s, 5p, 5d, 6s, 6p) with an energy cutoff on the wavefunctions of 60 Ryd and a 2×2×2 k-points grid in the Brillouin Zone. To check the validity of our model, we investigated both the bulk properties of SnO_2 with different levels of theory, comparing calculated results with the experimental data.

Table S1. Valence band (VB), conduction band (CB) level and band gap (eV, vs. vacuum) of bulk and 110 slab SnO_2 at different levels of theory.

SnO_2		VB	CB	GAP
Bulk	PBE			1.21
	PBE+U			4.50
	PBE0			3.49
Exp[20]		-8.0	-4.5	3.5
Slab	PBE	-7.3	-6.46	0.84
	PBE+U	-9.92	-7.71	2.20
	PBE0	-8.86	-6.13	2.73

The computed electronic properties of SnO_2, presented in the table, demonstrate that the bulk band gap is well described, particularly when using the PBE0 functional, which yields a band gap (3.49 eV) in close agreement with the experimental value (3.5 eV).[20] However, modeling the (110) surface presents significant challenges. Despite employing the same computational approaches, the predicted band gap for the slab structure deviates considerably from the experimental reference, indicating a potential limitation in accurately capturing surface

electronic states. Nevertheless, the VB energy nicely compares with experimental values, suggesting that the band-gap underestimate is mainly due to CB lowering due to surface cut. This underestimate is thus to affect the quantitative alignment of unoccupied states in the following analysis.

Scanning Electron Microscopy

Surface SEM images were collected using an FEI Quanta 600 scanning electron microscope at 5 kV acceleration voltage, 96 pA current, and a spot size of 3.0.

Current Density-Voltage (J-V) Measurements on Devices

The photovoltaic devices were characterized in ambient conditions with the room temperature around 20~25°C and 25% relative humidity under AM 1.5G simulated sunlight generated by a class AAA WaveLabs Sinus-220 solar simulator, using a Keithley 2400 source meter. The intensity of the solar simulator was set to produce 100 mW/cm^2 equivalent irradiance using a certified KG3-filtered Si reference photodiode (Fraunhofer ISE). The voltage was swept at a rate of 0.32 V/s first from forward bias to reverse bias followed by a reverse sweep in the opposite scan direction. The minimum voltage was -0.2 V and the maximum voltage was 1.2 V. On each substrate, there were three devices with an area of 0.25 cm^2 and one larger device with an area of 1.00 cm^2. The areas were defined using black anodized aluminum shadow masks in direct contact with the glass side of the substrates within enclosed sample holders.

External Quantum Efficiency (EQE) Measurements

External quantum efficiency was acquired with a custom build Fourier transform photocurrent spectrometer utilizing a Bruker Vertex 80v Fourier Transform Interferometer. Devices were calibrated to a Newport-calibrated silicon reference solar cell with known external quantum efficiency and illuminated with an AM1.5 filtered solar simulator. Devices were masked with the same metal aperture masks as in the J-V measurements, with active areas 0.25 cm^2 and 1 cm^2.

85 °C N_2 Aging Box

The 85 °C thermal aging test was done on unencapsulated devices in a dark nitrogen atmosphere. Devices were put inside a home-built oven with temperature control set to 85°C (±3°C) and removed periodically to measure device performance under ambient conditions.

70 °C and 65 °C AM 1.5 Light-Soaking Box

The light aging tests were done on encapsulated devices in an ambient atmosphere at 70±5 °C and <1% relative humidity and AM1.5G full spectrum pulsed light ATLAS SUNTEST XLS+ aging box. The (1,700 W) xenon lamp is pulsed at 100 Hz and averaged off to 0.76 sun intensity. The half stack samples were aged under 65 °C but otherwise the same conditions as the devices. The aging box regulated the temperature of the cells by measuring the temperature on a black temperature standard and controlling fan-speed to actively cool the chamber with air flow when the temperature increases beyond the targeted set point and reduce fan-speed when the temperature drops below. The exact position of the black temperature standard within the chamber, with respect to the where the cells are located, influences the difference between the actual cell temperature and the black temperature standard. The position of the black standard was set such that the cell temperature, as monitored by adhering a thermocouple to the rear of a test cell, closely matched the temperature of the black temperature standard.

Peel Test

We follow a standard American Society for Testing and Materials (ASTM) for the peel test. Cross hatch patterns were made on the samples with a cross hatch cutter. The cutting edge was placed on the sample and pressed down gently. The cross hatch cutter was pulled across the film in one steady movement to make a series of parallel cuts approximately 20 mm long. Efficient pressure was applied to ensure cutting right through the coating to the surface of the substrate. Then the cutting edge was placed at a 90˚ angle to the first cut and the cross hatch pattern was repeated to create a lattice pattern on the film. The sample was brushed lightly several times, forward and backwards along the diagonals of the lattice, to remove debris. Then the sample was inspected to ensure that the cuts have penetrated all the way through the coating. Two complete turns of adhesive tape was removed, and an additional length of tape at a steady rate and a piece of approximately 75 mm of length was removed. The cut piece was centred over the lattice and smoothed into place using finger. The tape was firmly rubbed using an eraser on the end of a pencil to ensure good adhesion between the tape and the

coating. Within 90 seconds (± 30 seconds) of applying the tape, the tape was removed by pulling in a single smooth action at an angle of 180˚ to the coating surface. The coating adhesion was assessed by viewing the lattice of cuts to see how much material came off.

Additional Information

C_{60}-PA was synthesized following a modified literature procedure.[1] Diethyl (C_{60}-substituted)phenylphosphonate[1] (0.20 g, 0.20 mmol) was dissolved in dry 1,2-dichloroethane (75 mL) at 75 °C. Bromotrimethylsilane (0.21 mL, 1.61 mmol, 8 equivalents) was added, and the mixture was maintained at 75 °C for 14 hours. After completion, the reaction was quenched with water (10 mL), and volatiles were removed under reduced pressure. The resulting precipitate was filtered, washed with water and methanol, and dried under vacuum to afford C_{60}-PA as a brown solid (0.18 g, 95% yield). ^{1}H NMR as shown in **Figure S1** (300 MHz, $CDCl_3/CS_2/CD_3OD$) δ 7.82-7.67 (m, 4H), 4.91-4.85 (m, 2H), 4.21-4.17 (m, 1H), 2.67 (s, 3H). HRMS (ESI-MS) for $C_{69}H_{11}NO_3P$ $[M-H]^-$: calc m/z = 932.0482; found m/z = 932.0468. The MS data (**Figure S2**) are consistent with previously reported in the literature.[1]

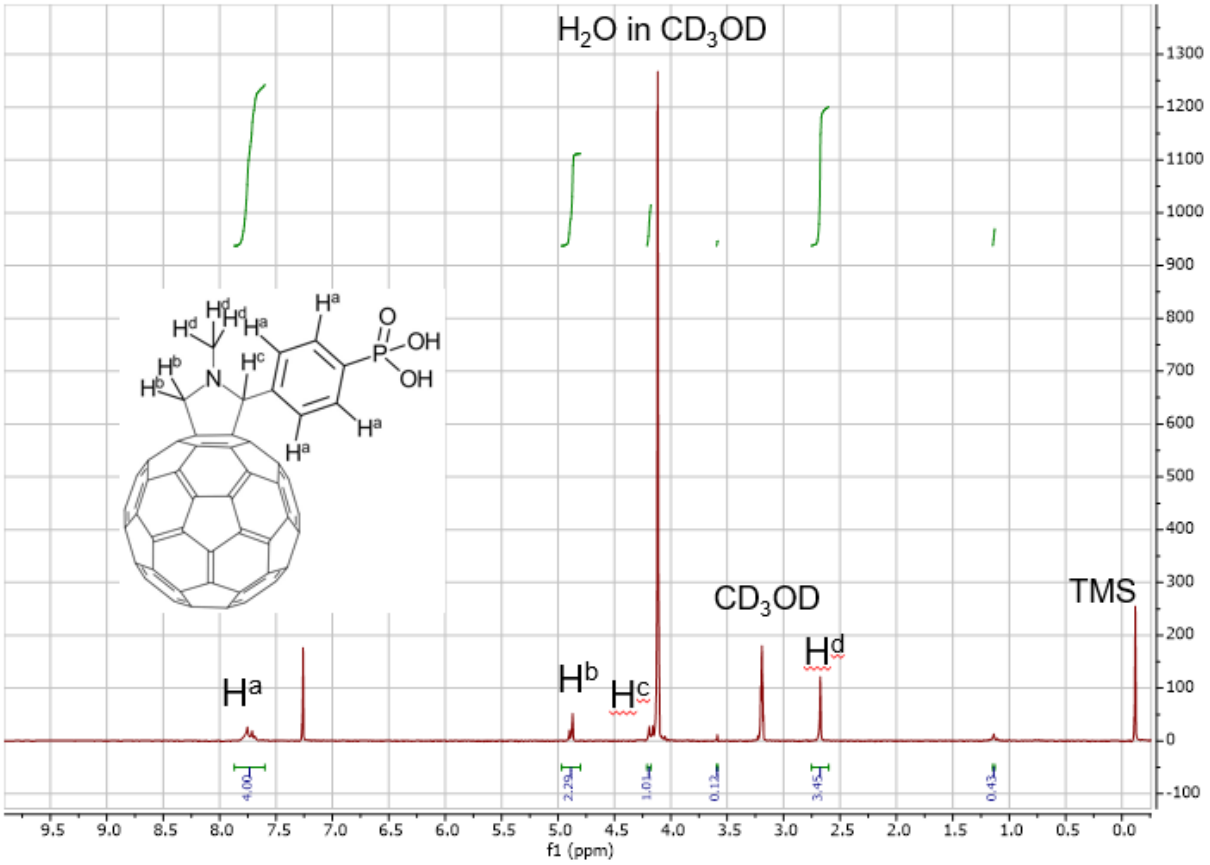

Figure S1. ^{1}H NMR of C_{60}-PA in $CDCl_3/CS_2/CD_3OD$.

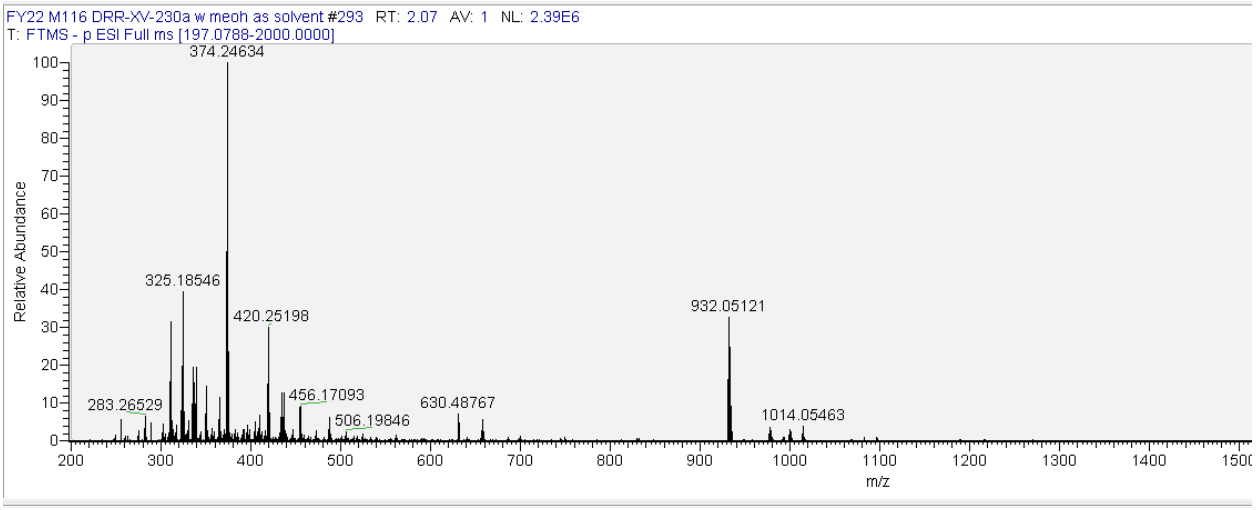

Figure S2. ESI-MS of C_{60}-PA, showing molecular ion (m/z) of 932.

We measured the UV-vis absorption spectrum of the C_{60}-PA and C_{60}-CA SAM-forming molecules in solution since the monolayers themselves are too weakly absorbing. The C_{60}-PA and C_{60}-CA SAMs exhibits absorption peaks at around 433 nm and 431 nm, respectively (**Figure S3**). As the SAMs are extremely thin (<1 nm), their parasitic absorption when used as ETLs is negligible. The C_{60} fullerene has a characteristic absorption peak at 404 nm, which arises from the electronic transition of the fullerene cage, specifically from the forbidden or weakly allowed π–π^* transitions associated with the conjugated carbon framework of the fullerene core.[21] However, in the fullerene derivatives, C_{60}-PA and C_{60}-CA, the presence of the electron-withdrawing functional groups (carboxylic acid and phosphonic acid) can perturb and shift the C_{60} core transition near 404 nm by lowering the energy of the Lowest Unoccupied Molecular Orbital (LUMO) of the C_{60} molecule,[22,23] which is involved in the electronic transition responsible for the absorption at that wavelength. This modification of the C_{60}'s electronic structure reduces the energy gap between the ground state and the excited state, resulting in a redshift to 433 nm and 431 nm. Note that the slight difference in this transition peak wavelength might also be influenced by the solvent used, with C_{60}-PA dissolved in DMSO and C_{60}-PA dissolved in 1:1 tetrahydrofuran: chlorobenzene.[24]

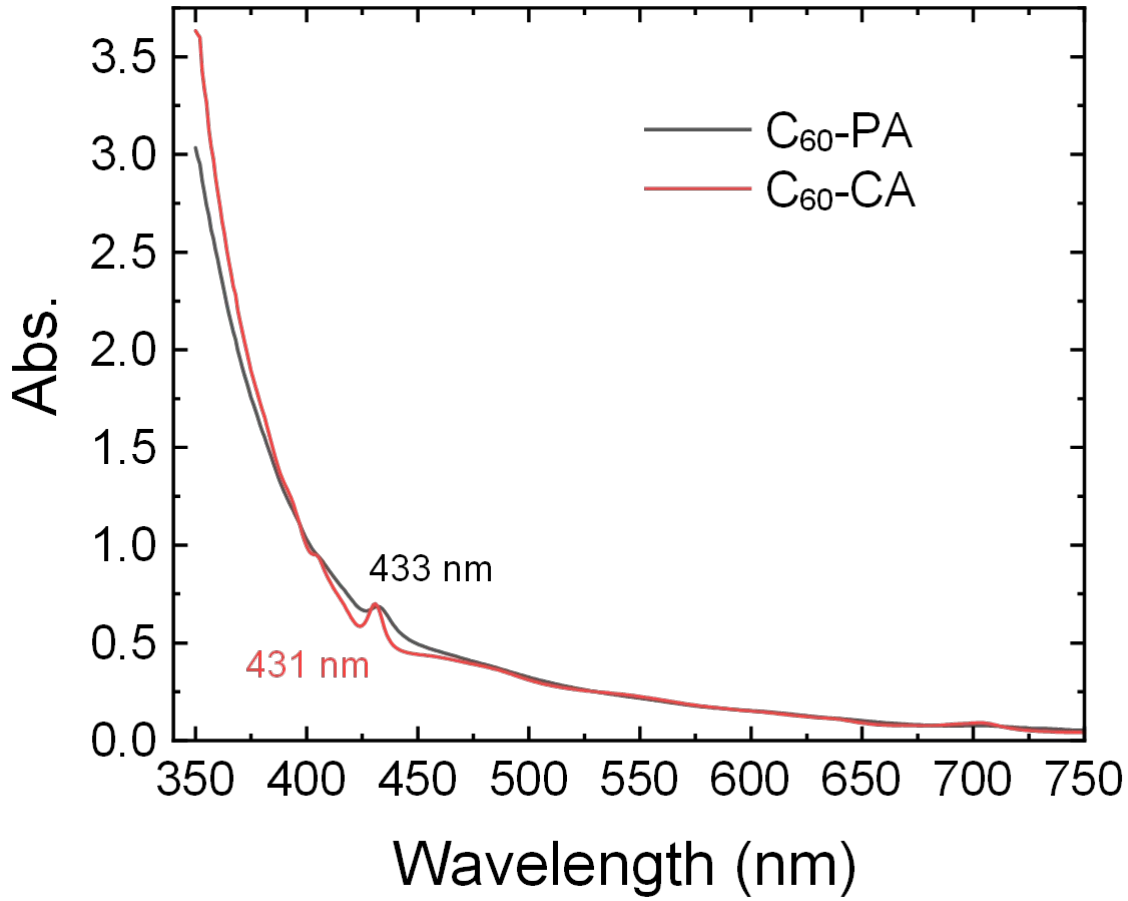

Figure S3. C_{60}-PA and C_{60}-CA absorption spectrum in solution, diluted to 0.2 mM.

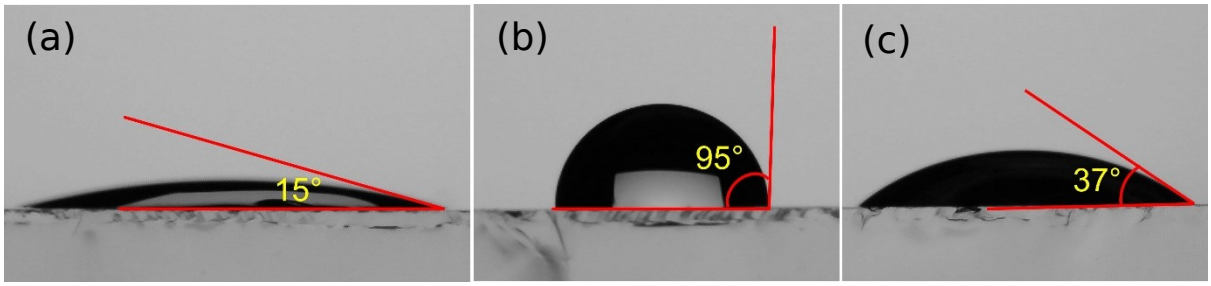

Figure S4. Contact angle measurement of water on (a) FTO (b) C_{60}-CA modified FTO 95° and (c) C_{60}-PA modified FTO 37°.

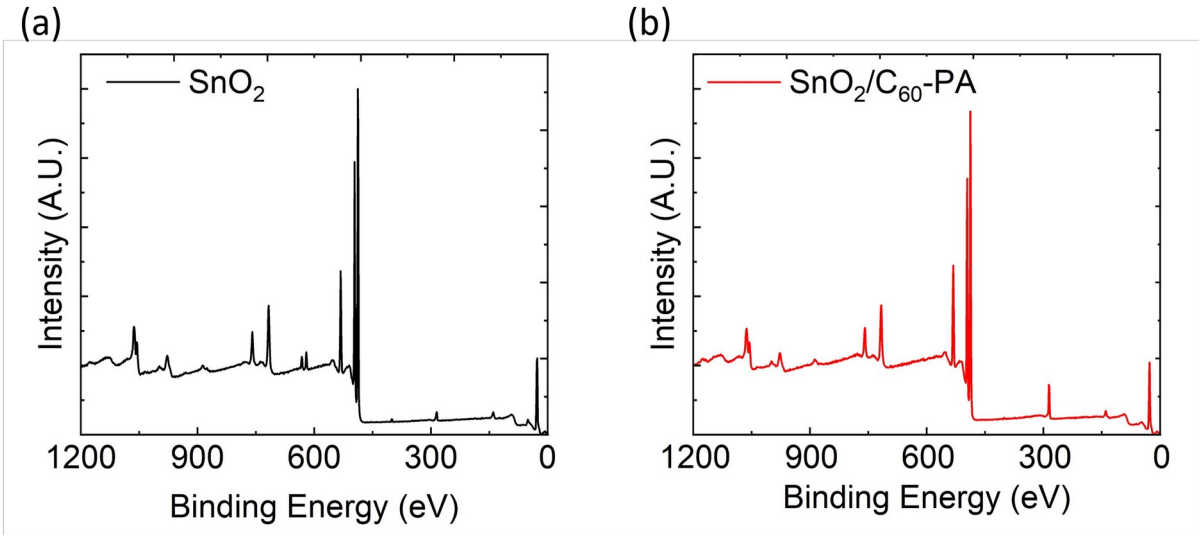

Figure S5. Survey scans used to calculate relative atomic composition of SnO_2 thin film (a) without and (b) with C_{60}-PA SAMs from X-ray photoelectron spectroscopy measurements.

Table S2. Elemental compositional analysis determined from X-ray photoelectron spectroscopy measurements. Compositional percentages were determined from survey scans and presented with ± standard deviation.

Elemental composition (%)	C 1s	O 1s	N 1s	Sn 3d
SnO_2	15.4 ± 0.5	61.6 ± 1.0	2.1 ± 0.6	20.6 ± 0.3
SnO_2/C_{60}-PA	42.8 ± 1.6	40.1 ± 4.3	0.9 ± 0.0	16.2 ± 3.3

The slightly higher nitrogen content on the SnO_2 surface compared to the SnO_2/C_{60}-PA could potentially be attributed to the high affinity that nitrogen oxide (NO_x) has to the SnO_2 surface and/or N_2 weakly adsorbed to the SnO_2. [25–29] Whereas such NO_x and N_2 adsorption could be reduced in the case where more SnO_2 surface site are occupied by C_{60}-PA.

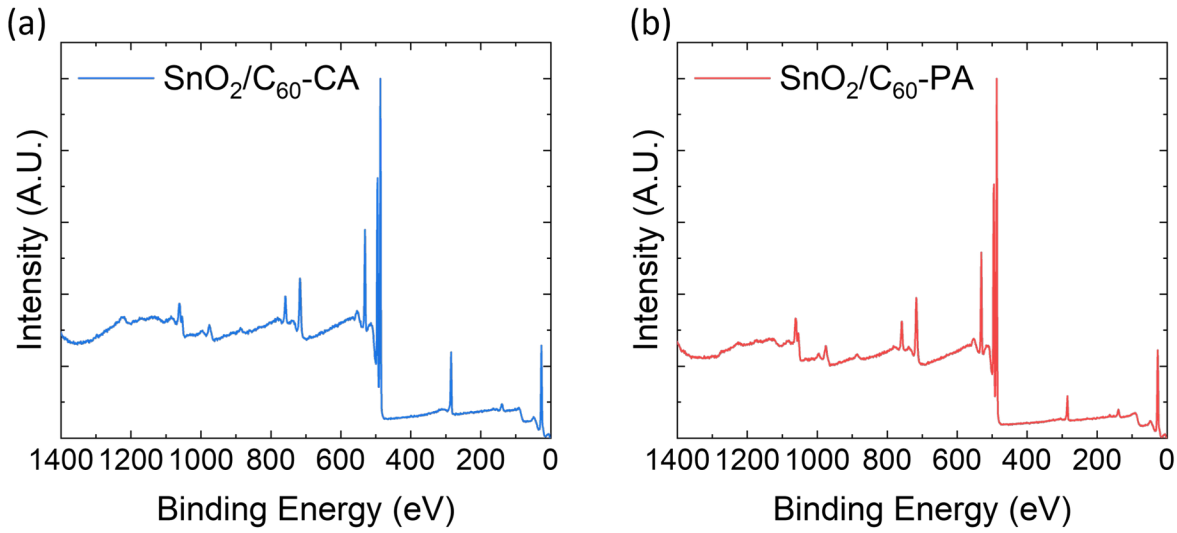

Figure S6. Survey scans used to calculate relative atomic composition of SnO_2 thin film (a) with C_{60}-CA and (b) C_{60}-PA SAMs from X-ray photoelectron spectroscopy measurements.

Table S3. Elemental composition comparison between SnO_2/C_{60}-PA and SnO_2/C_{60}-CA determined from XPS measurements. The analysis also shows trace amount of sulfur likely from the residual solvent for the SAMs, DMSO.

Elemental composition (atomic %)				
Sample	**O**	**Sn**	**C**	**S**
SnO_2/C_{60}-PA sample 1	45.7	27.4	25.8	1.1
SnO_2/C_{60}-PA sample 2	45.6	28.6	25	0.9
SnO_2/C_{60}-CA sample 1	34	20.7	44.6	0.7
SnO_2/C_{60}-CA sample 2	33	19.1	46.9	1.1

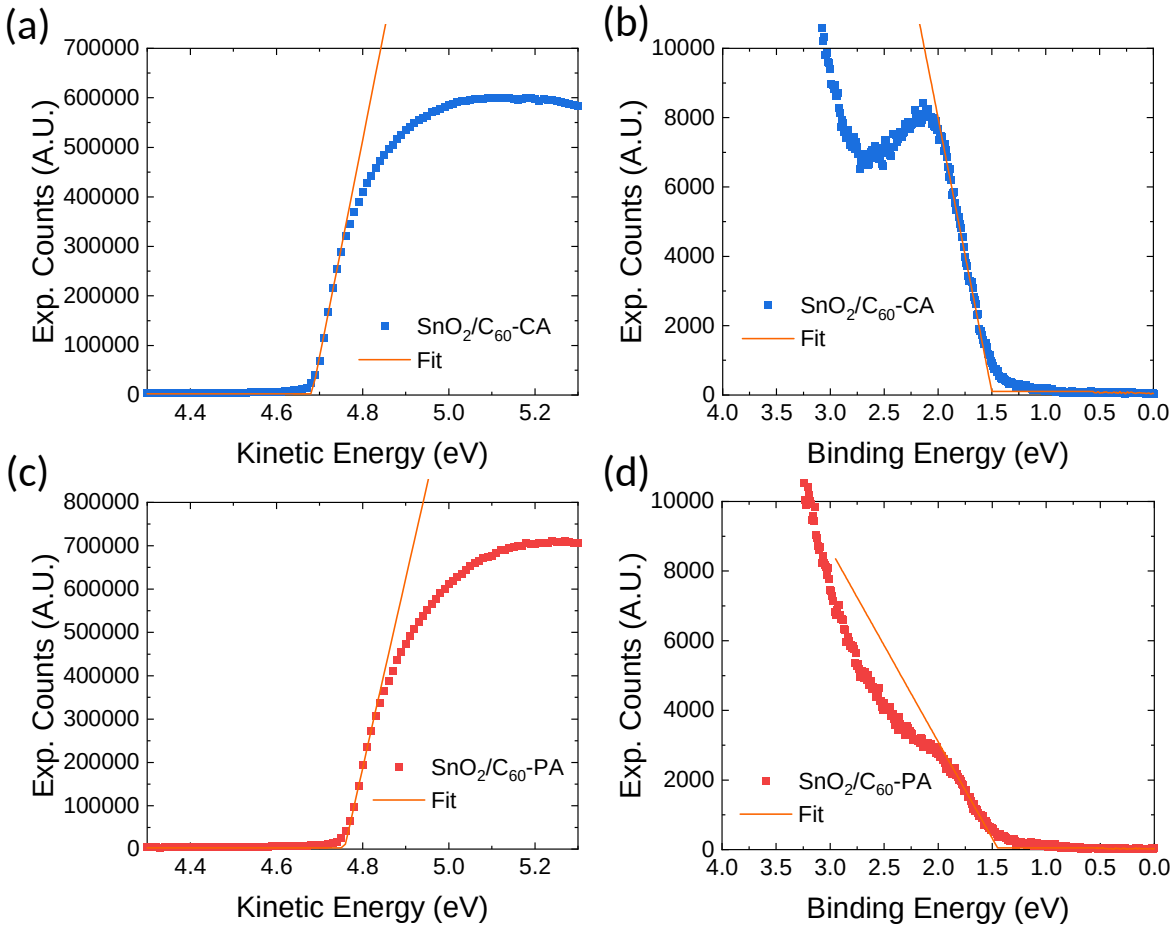

Figure S7. Ultraviolet photoelectron spectroscopy (UPS) measurements showing fitting of the (a) work function region of SnO_2/C_{60}-CA, (b) valence band onset region of SnO_2/C_{60}-CA, (c)

work function region of SnO_2/C_{60}-PA, (d) valence band onset region of SnO_2/C_{60}-PA. All samples were made on FTO glass substrates.

Table S4. Work function, secondary electron cut-off, valence band maximum, and ionization potential comparison between C_{60}-PA and C_{60}-CA.

Sample	Work function (eV)	Secondary electron cut-off (eV) [21.22 - WF]	Valence band maximum (eV)	Ionization Potential (eV)
C_{60}-PA 1	**4.7**	16.5	**1.4**	**6.1**
C_{60}-PA 2	**4.8**	16.5	**1.5**	**6.2**
C_{60}-CA 1	**4.5**	16.7	**1.5**	**6.0**
C_{60}-CA 2	**4.7**	16.5	**1.5**	**6.2**

Density Functional Theory Calculations

Interface simulations

We adsorb the functionalized fullerenes on top of the SnO_2 surface. The adsorption energy is calculated following the equation:

$$E_{ads} = E_{\int ¿ - E_{Sn\,O_2} - n E_{C\,60} ¿} \quad Equation\ S7$$

Where E_{ads} represents the energy for the interacting systems, E_{int} represents the total energy of the interacting system. E_{SnO2} is the energy of the clean surface and E_{C60} represents the energy of isolated different functionalized molecules optimized with the same computational approach. The adsorption energies are reported in **Table S5**.

Table S5. Adsorption energy per molecule (eV) for C_{60}, C_{60}-CA, and C_{60}-PA.

	E_{ads} (eV per molec.)		$\Delta\, full - half$
Coverage	*half*	*full*	
C_{60}	-3.01	-2.58	0.43
C_{60}-CA	-5.78	-5.41	0.37
C_{60}-PA	-6.97	-6.21	0.76

Electronic properties

We study the electronic properties with DFT, focusing our attention on the energy positions alignment of the valence band maxima (VBM) on differently interacting SnO_2 surfaces**.** The

VBMs were quantified by calculating the associated ionization energy (*IE*). The *IE* is defined here as the energy required to extract electrons from the valence band and is distinguished from the work function of the slab, which is the energy required to extract electrons from the Fermi level and is significantly influenced by carrier densities and surface defects. *IE*s have been calculated by using the expression:

$$IE = E(vac) - E(VMB) \qquad \textbf{Equation S8}$$

In **Equation S8**, *E(vac)* is the potential in the vacuum, i.e. the sum of the pseudo and Hartree potentials (*VPS* + *VH*) in the vacuum region between periodic slabs, and *E(VBM)* is the energy of the top of the valence band. The hybrid PBE0 functionals were used to calculate ionization energies (*IE*s). We first investigated the energy level alignment of the organic components after structural optimization. To this end, the SnO_2 substrate was effectively "removed" and the HOMO-LUMO positions of the organic SAMs were analyzed.

Table S6. Energy level of the organic part removed from the interacting system.

	Fullerene layer cut from interface					
Coverage	half			full		
	HOMO	LUMO	Gap	HOMO	LUMO	Gap
C_{60}	-6.57	-3.67	2.90	-6.22	-3.95	2.27
C_{60}-CA	-5.82	-3.91	1.91	-5.76	-4.04	1.72
C_{60}-PA	-5.70	-3.78	1.92	-5.41	-3.88	1.53

Table S7. Energy level of the SnO_2 and organic from the interacting system and the total interface level alignment in the interacting system.

	Interface Half Coverage						**Interface Full Coverage**					
Coverage	SnO_2			Organic			SnO_2			Organic		
	VBM	CBM	Gap	H	L	Gap	VBM	CBM	Gap	H	L	Gap
C_{60}	-8.47	-6.03	2.44	-6.58	-3.75	2.83	-8.57	-6.00	2.57	-6.47	-4.07	2.40
C_{60}-CA	-8.54	-6.07	2.48	-6.41	-4.54	1.87	-8.67	-6.01	2.66	-6.41	-4.62	1.79
C_{60}-PA	-8.53	-6.08	2.45	-6.41	-4.54	1.87	-8.71	-6.06	2.65	-6.09	-4.58	1.51

As illustrated in **Table S6**, we observed that increasing the molecular coverage of C_{60} brought our calculated ionization potential (-6.22 eV) closer to the experimentally measured value of -6.12 eV for a thin fullerene film. Increasing molecular coverage leads to a shift in the valence band toward higher energies (becoming less negative), while the conduction band becomes more stabilized. Consequently, this leads to a reduction in the band gap of the organic material. This trend is further illustrated by the findings presented in **Table S6**, which examines the electronic structure of the interacting systems, emphasizing the impact of molecular density on energy level alignment.

Table S7, as well depicted from the projected density of states in **Figure S8**, shows how increasing the molecular coverage on the SnO_2 surface, from half to full coverage, allows us to reproduce the trend observed experimentally by UPS measurements. Specifically, UPS data indicate that the C_{60}-CA exhibits a deeper valence band compared to C_{60}-PA. This finding is consistent with the valence band maximum (VBM) that was computationally determined, which corresponds to the HOMO level of the molecule—the highest occupied level from which electrons can be removed from the interacting system. At full coverage, the calculated VBM values are -6.41 eV and -6.09 eV for C_{60}-CA and C_{60}-PA, respectively, confirming that C_{60}-CA has a deeper energy level than C_{60}-PA. It is important to note that this outcome is only observed when the molecular density is increased on the SnO_2 surface. This is due to the fact that the interaction at higher coverage influences the electronic properties of the overall system.

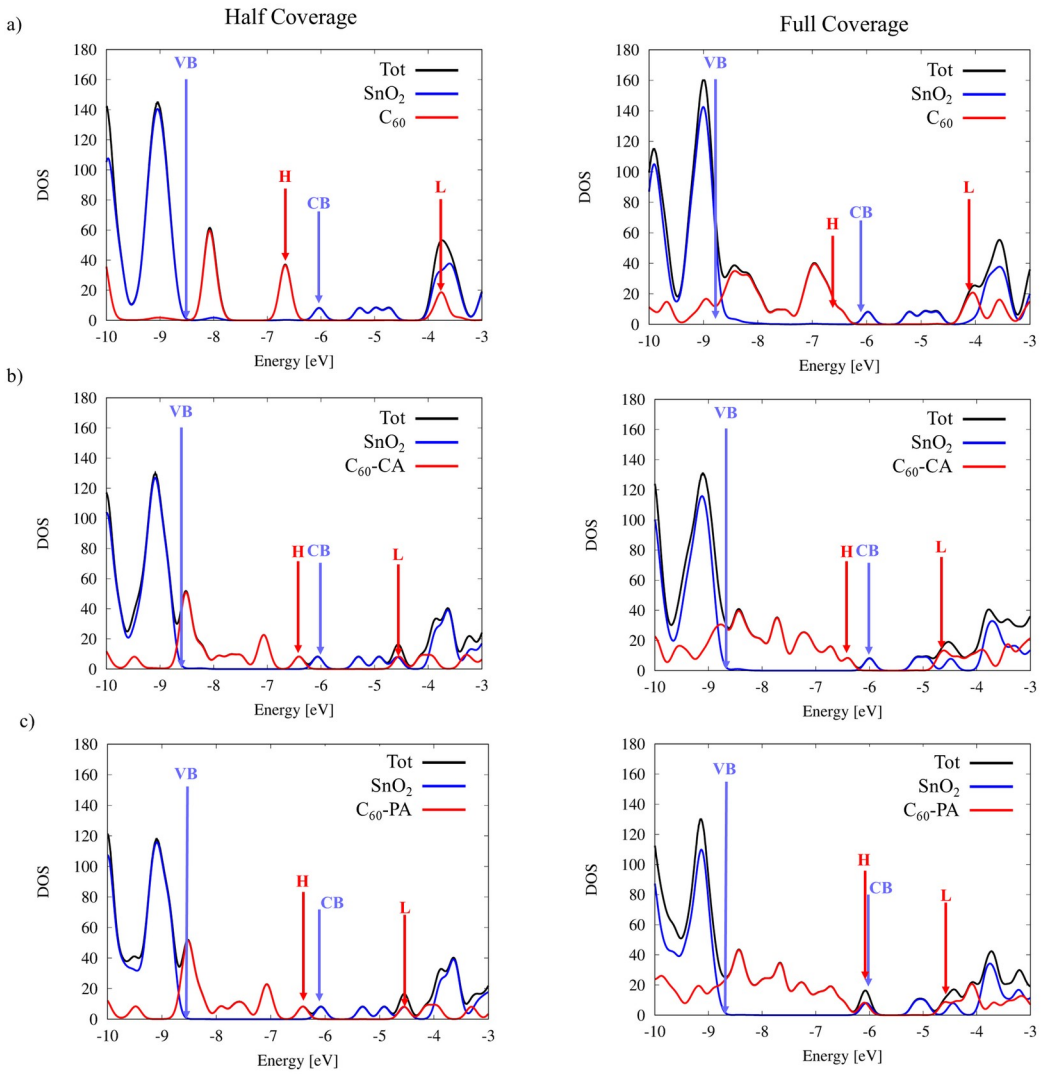

Figure S8. Density of states of the interface between SnO_2 with (a) C_{60}, (b) C_{60}-CA and (c) C_{60}-PA with the separated projected density of states (PDOS) contribution of the inorganic part (blue) and organic part (red). All the PDOS are calculated at the PBE0-D3 level of theory.

Moreover, we carried out additional calculations on the molecular systems by the means of Gaussian09 package [30,31]. We calculated the Molecular Electrostatic Potentials for both the systems on the optimized geometry obtained from the surface calculations. We employed hybrid PBE0[18] functional with 6-311G* basis set [30,31] to be as accurate as possible with the technical details used in the periodical calculation. Finally, we also computed the dipole moment on the same optimized structure reported in **Figure 1**.

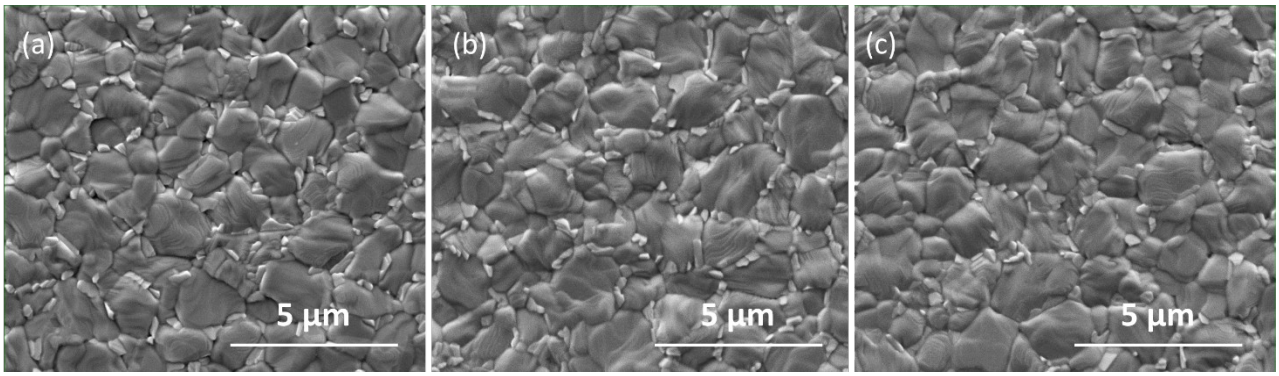

Figure S9. Top-view scanning electron microscopy (SEM) images of $FAPbI_3$ processed on (a) FTO/SnO_2, (b) FTO/SnO_2/C_{60}-CA, (c) FTO/SnO_2/C_{60}-PA.

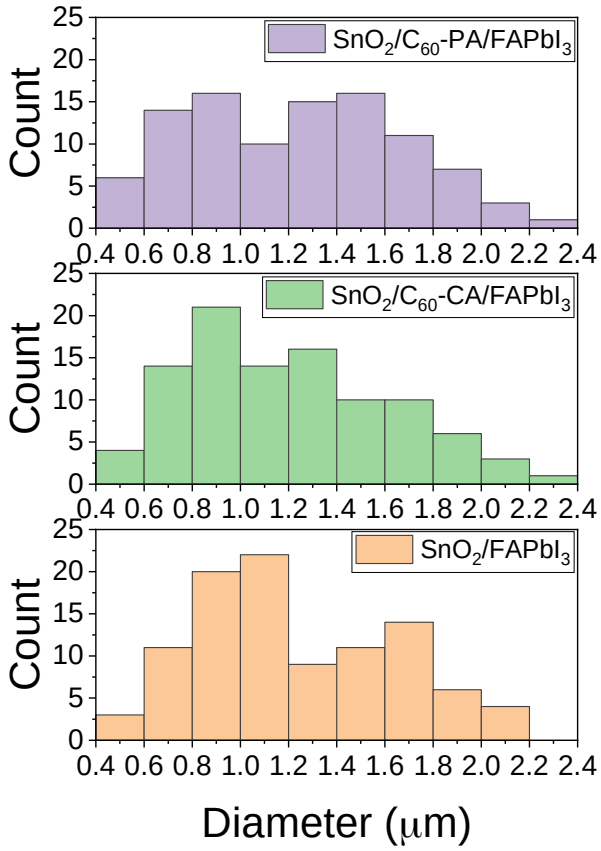

Figure S10. Grain size analysis according to SEM images from **Figure S9**. The diameters of the grains were measured in ImageJ.

Table S8. Average diameter of the perovskite grains ± standard deviation.

Thin Film	**SnO_2/$FAPbI_3$**	**SnO_2/C_{60}-CA/$FAPbI_3$**	**SnO_2/C_{60}-PA/$FAPbI_3$**
Grain Diameter (µm)	1.24 ± 0.42	1.22 ± 0.44	1.26 ± 0.46

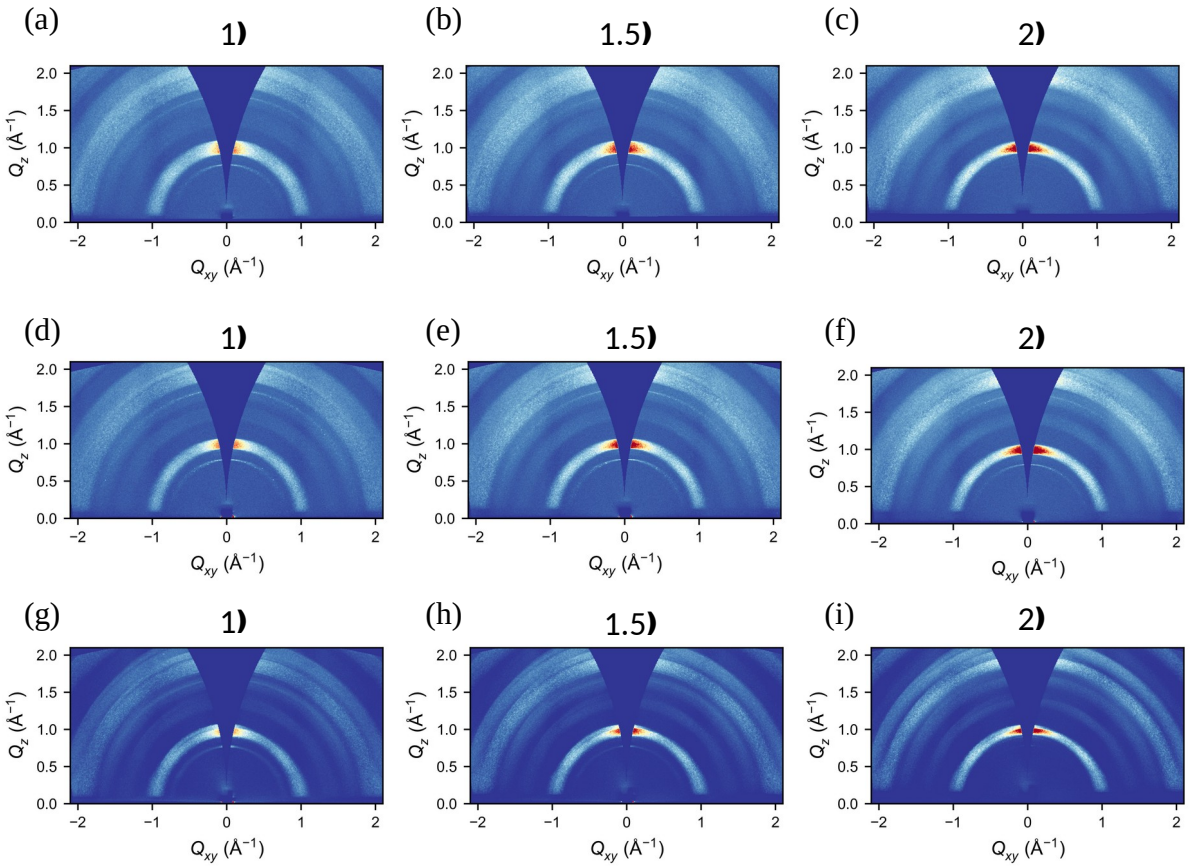

Figure S11. GIWAXS patterns of $FAPbI_3$ (with MACl and $MAPbBr_3$) perovskite grown on (a)-(c) SnO_2, (d)-(f) SnO_2/C_{60}-CA, and (g)-(i) SnO_2/C_{60}-PA from 1˚~2˚ incident angles.

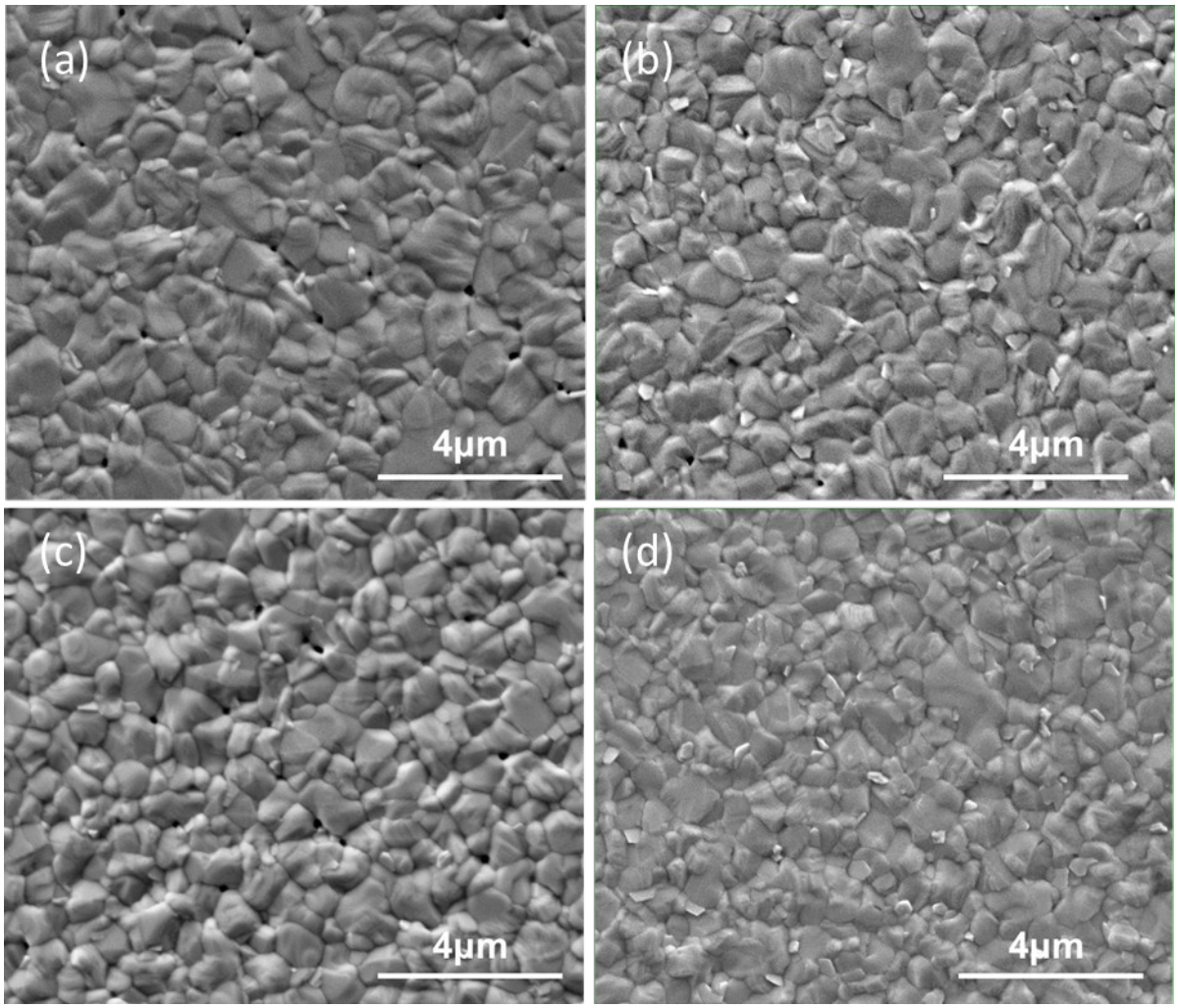

Figure S12. Top-view scanning electron microscopy (SEM) images of $FAPbI_3$ processed on (a) FTO (b) FTO/SnO_2 (c) FTO/C_{60}-PA (d) FTO/SnO_2/C_{60}-PA.

Note S1:

We further analyze the ETL/perovskite interface to understand how the C_{60}-SAMs might affect charge transport. We perform time-correlated single photon counting (TCSPC) on "half-stack" samples either with or without C_{60}-SAM modification (**Figure 1 e**). Stretched exponential decay fitting was applied to extract their charge-carrier lifetime, τ. Here we use a stretched-exponential decay fitting function to fit the PL decay. [32–36]

$$I(t) = A_1 e^{-\left(\frac{t}{\tau c}\right)^{\beta}}$$

Where A_1 is a pre-exponential factor, τ_c is the characteristic lifetime, and β is the stretching factor. β values can range from 0 to 1, with values closer to 1 indicating a more homogeneous carrier lifetime distribution and values closer to 0 indicating a more heterogeneous distribution. The average lifetime can then be calculated from τ_c and β according to equation as reported before. [32]

$$\langle \tau \rangle = \frac{\tau_c}{\beta} \Gamma\left(\frac{1}{\beta}\right)$$

The gamma function is defined as

$$\Gamma\left(\frac{1}{\beta}\right) = \int_0^\infty x^{\frac{(1-\beta)}{\beta}} e^{-x} dx$$

This integral arises from the distribution of superposition of exponentials and hence take into account the heterogenous nature of the various “pixel” points emitting PL.

According to the fitting results in **Figure S13**, summarized in **Table S9**, τ is higher for the C_{60}-CA-modified half-stack but lower for the C_{60}-PA-modified half stack. The lower PL lifetime of C_{60}-PA could be due to either: (1) the presence of a PA SAM accelerating charge-carrier extraction at the SnO_2/perovskite interface resulting in accumulation at the contacts instead of recombining in the perovskite absorber layer; or (2) the C_{60}-PA layer increasing the rate of non-radiative recombination at the interface.

(a)

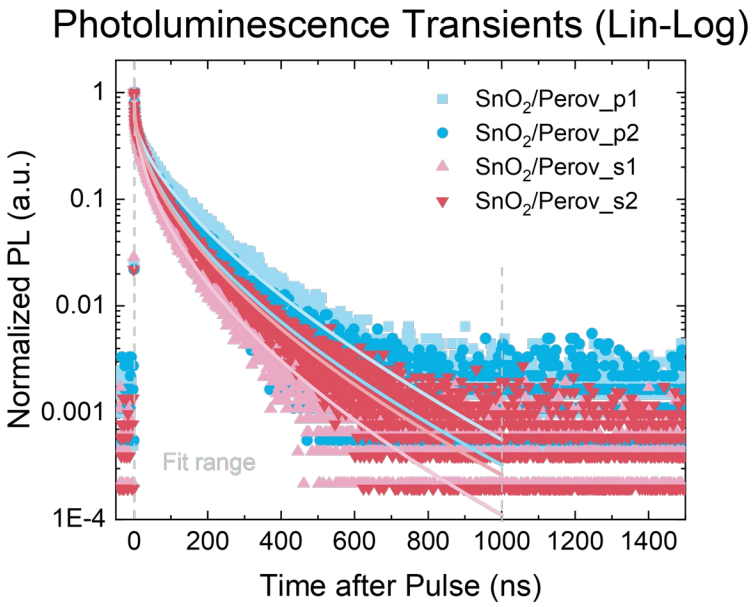
Photoluminescence Transients (Lin-Log)
Normalized PL (a.u.)
1
0.1
0.01
0.001
1E-4
0
200
400
600
800
1000
1200
1400
Time after Pulse (ns)
SnO2/Perov_p1
SnO2/Perov_p2
SnO2/Perov_s1
SnO2/Perov_s2
Fit range

(b)

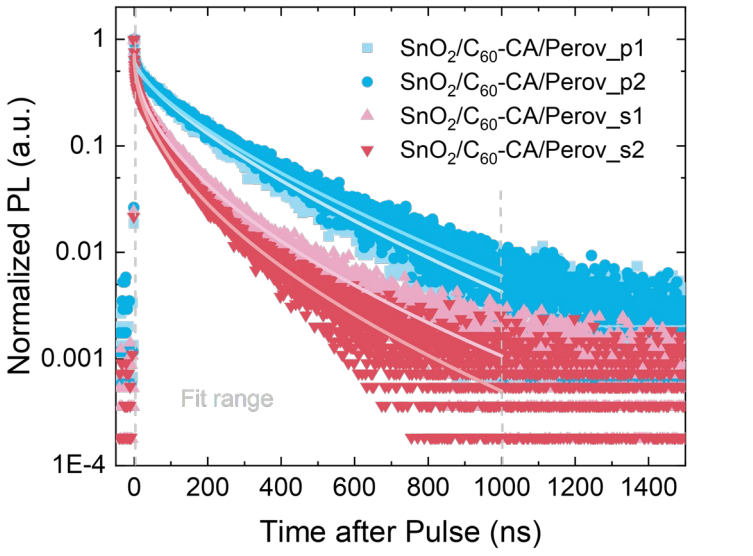
Photoluminescence Transients (Lin-Log)
Normalized PL (a.u.)
1
0.1
0.01
0.001
1E-4
0
200
400
600
800
1000
1200
1400
Time after Pulse (ns)
SnO2/C60-CA/Perov_p1
SnO2/C60-CA/Perov_p2
SnO2/C60-CA/Perov_s1
SnO2/C60-CA/Perov_s2
Fit range

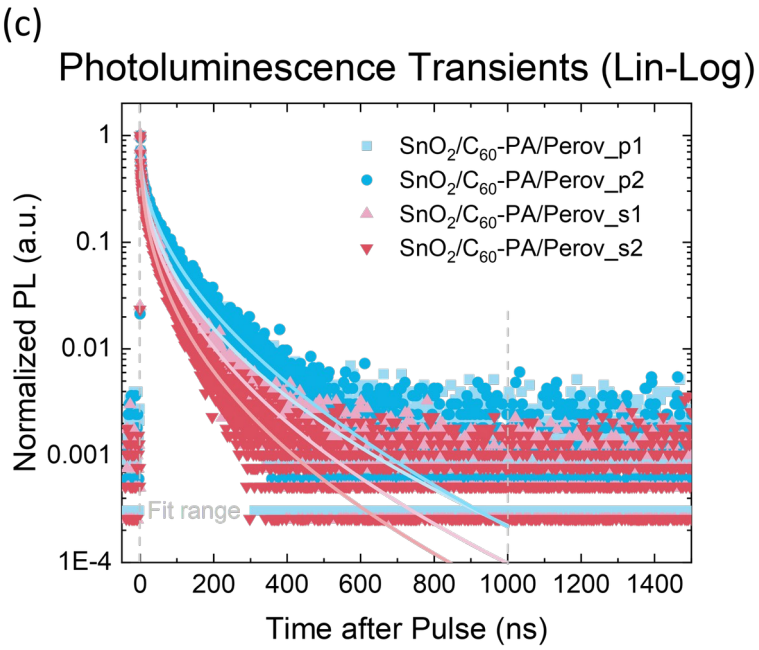

Figure S13. Time-resolved photoluminescence of (a) FTO/SnO_2/perovskite samples, (b) FTO/SnO_2/C_{60}-CA/perovskite samples, and (c) FTO/SnO_2/C_{60}-PA/perovskite samples. p1 indicates first point measured from the perovskite side, p2 indicates second point measured from the perovskite side, s1 indicates first point measured from substrate side, and s2 indicates second point measured from substrate side.

Table S9. Charge carrier lifetime and β factor (average ± standard deviation) of ETL/perovskite bilayer stack determined by stretched-exponential decay fitting. The results are the average of the two measurements made from the substrate side.

	τ (ns)	**β**
FTO/SnO_2/$FAPbI_3$	32.5±8.7	0.53±0.03
FTO/SnO_2/C_{60}-CA/$FAPbI_3$	45.6±9.9	0.52±0.02
FTO/SnO_2/C_{60}-PA/$FAPbI_3$	13.3±3.4	0.42±0.01

Note S2:

To understand the lower PL lifetime of C_{60}-PA could be due to reasons (1) or (2) in **Note 1**, we measure the photoluminescence quantum yield (PLQY) of the bilayer materials stack. As shown in **Figure S14**, the difference among SnO_2/$FAPbI_3$, SnO_2/C_{60}-CA/$FAPbI_3$, and SnO_2/C_{60}-PA/$FAPbI_3$ is small, yet they are consistent with the TRPL result of C_{60}-PA reducing the PL luminescence.

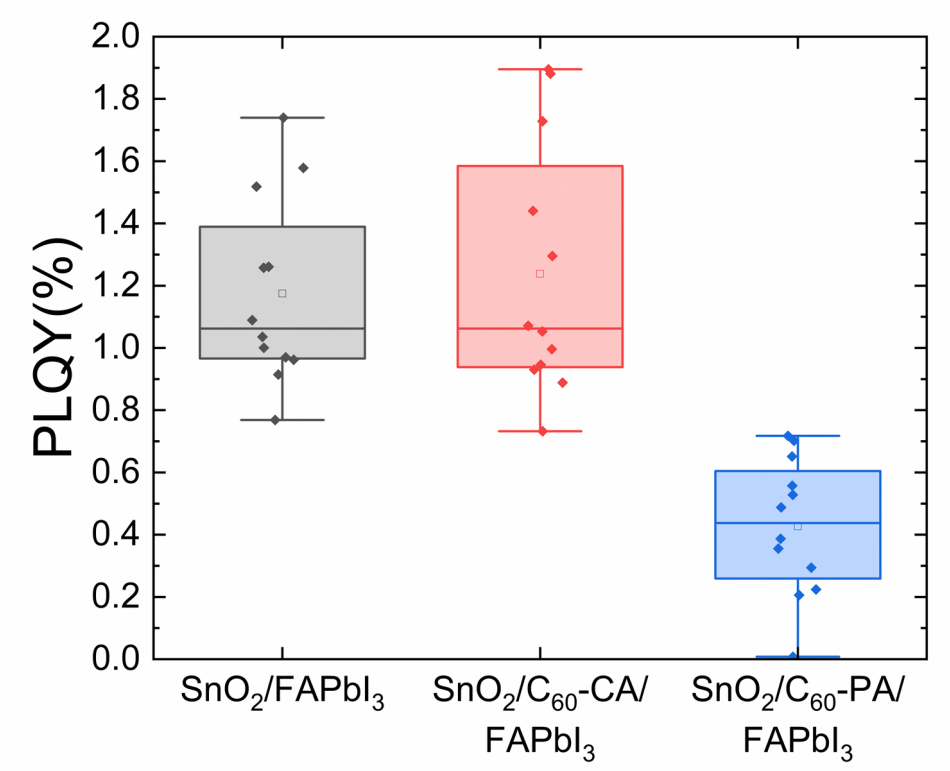

Figure S14. PLQY of ETL/perovskite half stacks measured with a 532 nm laser under 1 sun equivalent intensity.

Note S3:

We further carried out time-resolved surface photovoltage (tr-SPV) on SnO_2/C_{60}-PA and the control sample. In **Figure S15** we show the transient SPV signal of the half stacks following photoexcitation with 620 nm pulsed laser. Positive SPV signals are observed, consistent with electrons separated at the ETL/perovskite interface, resulting in a net positive charge closer to the surface due to accumulation of the remaining holes. Interestingly, under low fluence (1-sun intensity) (**Figure S15 a**), following a near-immediate increase of the SPV signal, after 10-20 ns we observe a significant delay in the rise in SPV signal for the SnO_2/C_{60}-PA sample, as compared to the SnO_2 sample, with the peak in the SPV signal shifting from sub-microseconds to the order of ten microseconds. Since charge transport and charge transfer should occur on the ns timescale,[12,37] this SPV rise is most likely to originate from the build-up of trapped surface charges. The delayed SPV rise for the SAM-modified sample, therefore, indicated an increased density, or an increased energetic depth, of surface trap states.[38]

At low light intensity (low carrier injection), we infer charge trapping and delayed charge extraction, from the overall lower rise time of the surface photovoltage signal. This is indicative of the trapped electrons being released, likely because the trapped electrons are recombining with nearby holes non-radiatively; however, under high light intensity (high carrier injection) (**Figure S15 b**), the traps are filled up by excess electrons, so we do not observe delayed SPV response. This phenomenon is observed in other fullerene derivatives with perovskites and is thought to be a dominant voltage-loss mechanism in p-i-n PSCs with fullerene ETLs.[39–42] Overall, while the perovskite grown on C_{60}-PA modified SnO_2 show similar grain orientation and morphology to perovskite grown on C_{60}-CA modified SnO_2 and SnO_2, yet we see evidence for temporary electron trapping at the ETL/perovskite interface. Considering the molecular electrostatic potential map of the C_{60}-SAMs in **Figure 1 c**, electrons move from low electric potential to high electric potential which indicates that electrons may localize at the C_{60} and pyrrole group before being transferred to the SnO_2.

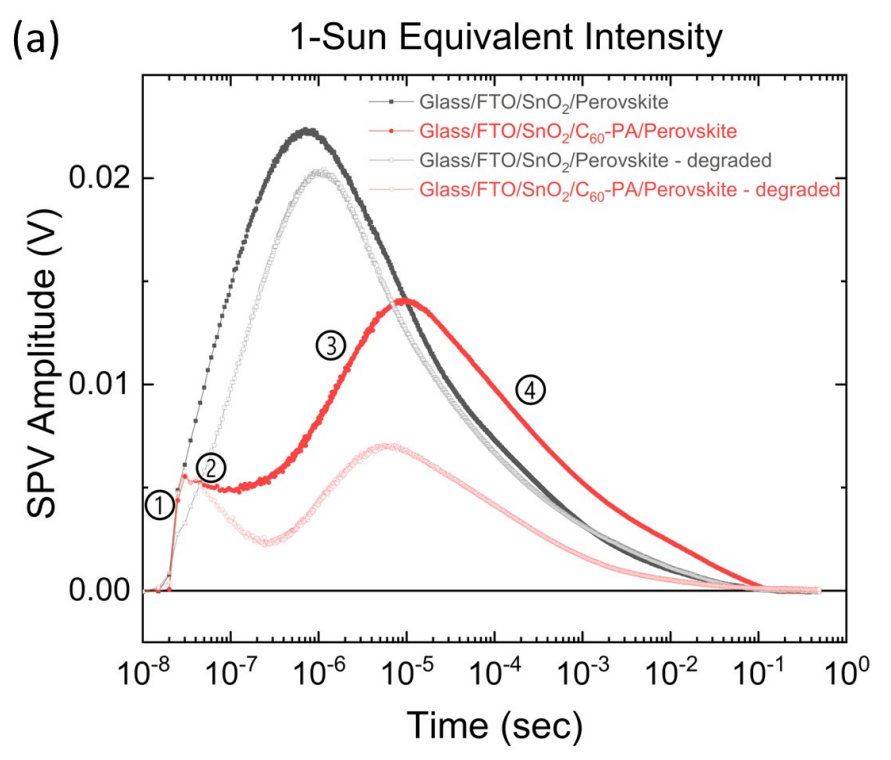

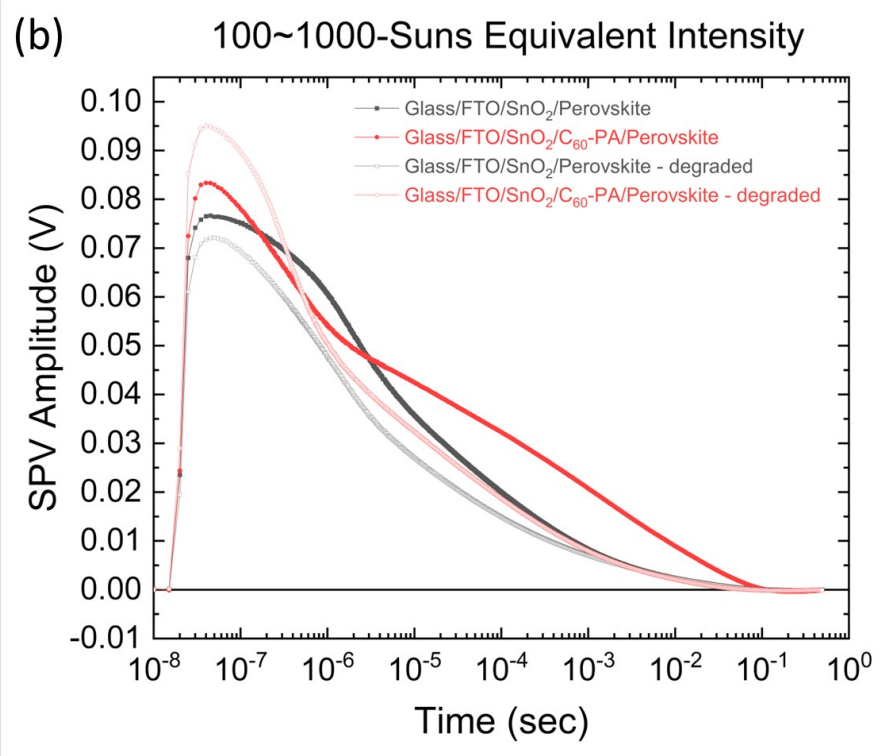

Figure S15. Surface photovoltage of ETL/$FAPbI_3$ perovskite samples measured from the glass side under (a) low-intensity 1-sun intensity light, ① e^- moving to the ETL interface. ② trapping of e^- at the ETL interface and e^--h^+ recombination. ③ release of trapped e^-. ④ recombination of de-trapped e^--h^+ pairs and back-transferred charge carriers. (b) high-intensity 100~1000 suns equivalent intensity light. Laser excitation at 620 nm and one-sun intensity with a 2 Hz repetition rate. Degraded samples are samples (unencapsulated) aged for 24 hours under an AM 1.5G spectrum 0.76 suns intensity xenon lamp under 65 °C and ~30% RH.

Note S4:

We fabricate negative-intrinsic-positive (n-i-p) devices with the architecture: FTO/SnO_2/(with or without) C_{60}-PA/$FAPbI_3$/PEAI/Spiro-OMeTAD/Au. The steady-state device parameters are summarized in **Figure S16**. While the steady-state short-circuit current density (ssJ_{sc}) and steady-state open circuit voltage (ssV_{oc}) are similar for the control devices and devices with SAM modification, the steady-state fill factor (ssFF) increased ~5% with the SAM modification. As a result of the ssFF enhancement, the overall average maximum power point tracked efficiency (η_{MPPT}) improved from 18.6% to 20.0%. As shown in **Table S10**, the J-V curves of champion n-i-p devices with or without C_{60}-PA modification are similar, with smaller difference between the forward and reverse scan for the C_{60}-PA treated device.

The external quantum efficiency (EQE) in **Figure S16(f)** also shows similar response for both devices, confirming the lack of difference in their current densities. The champion device parameters are summarized in **Table S11**. These results agree with the fact that we only observe small differences in the PL lifetime or PLQY (approximately halving) between the bilayer stacks without and with C_{60}-PA and hence do not expect a difference in open-circuit voltage due to this interface, beyond around 30 meV.

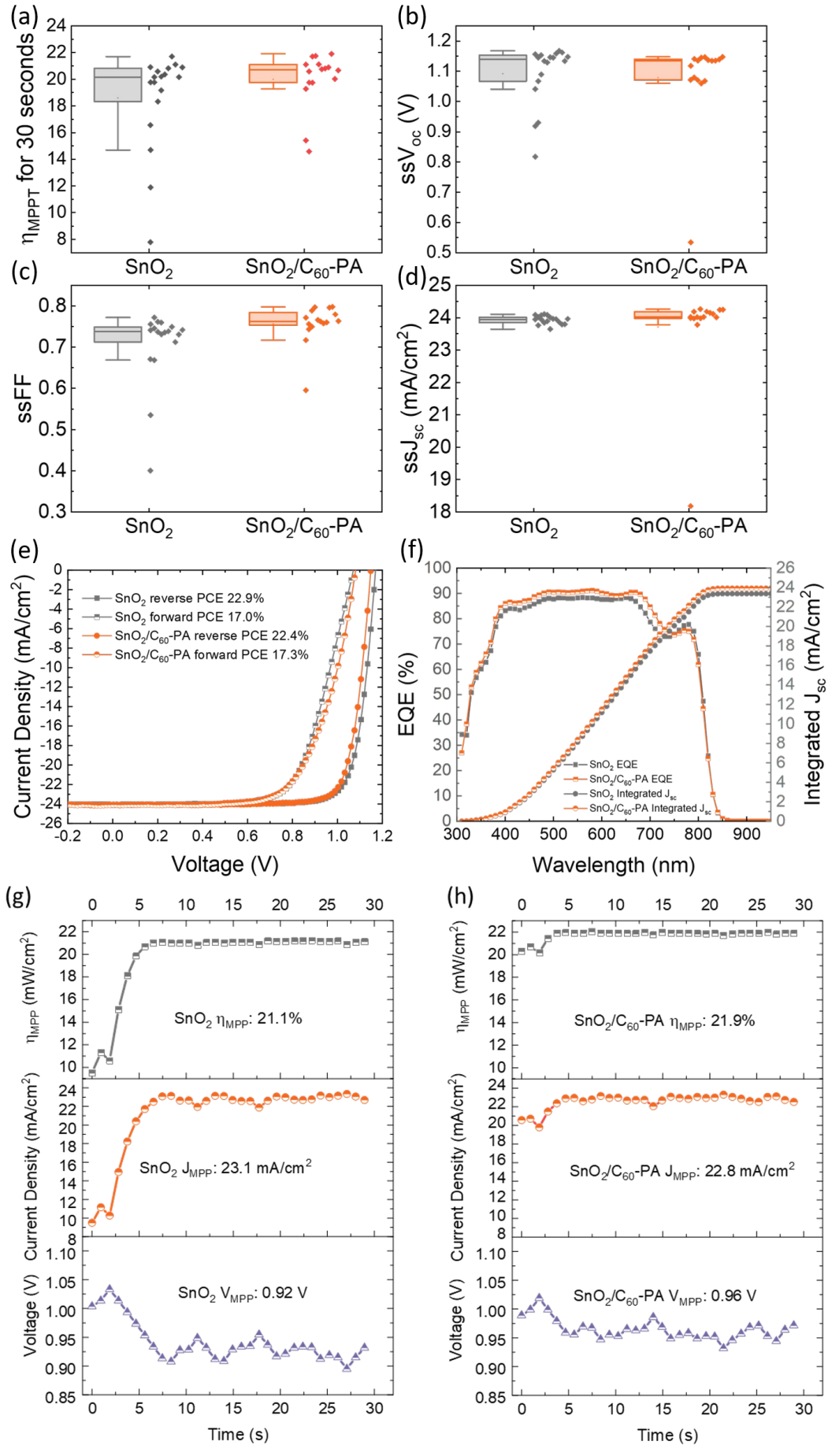
(a)
η_{MPPT} for 30 seconds
SnO2
SnO2/C60-PA
(b)
ssVoc (V)
SnO2
SnO2/C60-PA
(c)
ssFF
SnO2
SnO2/C60-PA
(d)
ssJsc (mA/cm2)
SnO2
SnO2/C60-PA
(e)
Current Density (mA/cm2)
SnO2 reverse PCE 22.9%
SnO2 forward PCE 17.0%
SnO2/C60-PA reverse PCE 22.4%
SnO2/C60-PA forward PCE 17.3%
Voltage (V)
(f)
EQE (%)
Integrated Jsc (mA/cm2)
SnO2 EQE
SnO2/C60-PA EQE
SnO2 Integrated Jsc
SnO2/C60-PA Integrated Jsc
Wavelength (nm)
(g)
ηMPP (mW/cm2)
SnO2 ηMPP: 21.1%
Current Density (mA/cm2)
SnO2 JMPP: 23.1 mA/cm2
Voltage (V)
SnO2 VMPP: 0.92 V
Time (s)
(h)
ηMPP (mW/cm2)
SnO2/C60-PA ηMPP: 21.9%
Current Density (mA/cm2)
SnO2/C60-PA JMPP: 22.8 mA/cm2
Voltage (V)
SnO2/C60-PA VMPP: 0.96 V
Time (s)

Figure S16. Box plot of device parameters with and without C_{60}-PA modified SnO_2. (a) maximum power point tracked efficiency for 30 s. (b) Steady-state open-circuit voltage (ssV_{oc}) for 30 s. (c) Steady-state fill factor (ssFF) for 30 s. (d) Steady-state current density (J_{sc}) for 10 s. (e) Forward and reverse J-V sweeps of devices with or without C_{60}-PA modification. (f) External quantum efficiency (EQE) spectrum (left) and integrated short-circuit current density (right) of devices with or without C_{60}-PA modification. Maximum power point-tracked efficiency for 30 s of (g) SnO_2 devices and (h) SnO_2/C_{60}-PA devices. The final η_{MPP} is the average of the MPP measured in the last 5 s of tracking.

Table S10. The statistical parameters of n-i-p devices made with and without C_{60}-PA modifications, average ± standard deviation.

Device ETL	**ssJ$_{sc}$ (mA/cm^2)**	**ssVoc (V)**	**ssFF**	**η_{MPPT} (%)**
FTO/SnO_2	23.9 ± 0.1	1.09 ± 0.10	70.5 ± 9.3	18.6 ± 3.7
FTO/SnO_2/C_{60}-PA	23.7 ± 1.5	1.08 ± 0.15	75.6 ± 4.8	20.0 ± 2.1

Table S11. Champion device parameters measured under a voltage sweep speed of 0.32 V/s.

Device ETL	**Scan Direction**	**Jsc (mA/cm2)**	**Voc (V)**	**FF (%)**	**PCE (%)**	**η_{mpp}**
SnO_2	Reverse	24.0	1.16	82.0	22.9	21.1
	Forward	24.0	1.05	67.4	17.0	
SnO_2/C_{60}-PA	Reverse	24.1	1.15	81.1	22.4	21.9
	Forward	24.1	1.08	66.6	17.3	

Note S5:

We note that the values of the $J_{sc,}$ and hence efficiency, should not be taken as absolute, since our light source for the frequency dependent J-V curves is not as well calibrated as our AM 1.5G solar simulator. Furthermore, the absolute values of the *FF*, and hence efficiency, are lower than in the solar simulator measurement because there is an 11 Ω resistor in series with the solar cell which increases the perceived solar cell resistance.

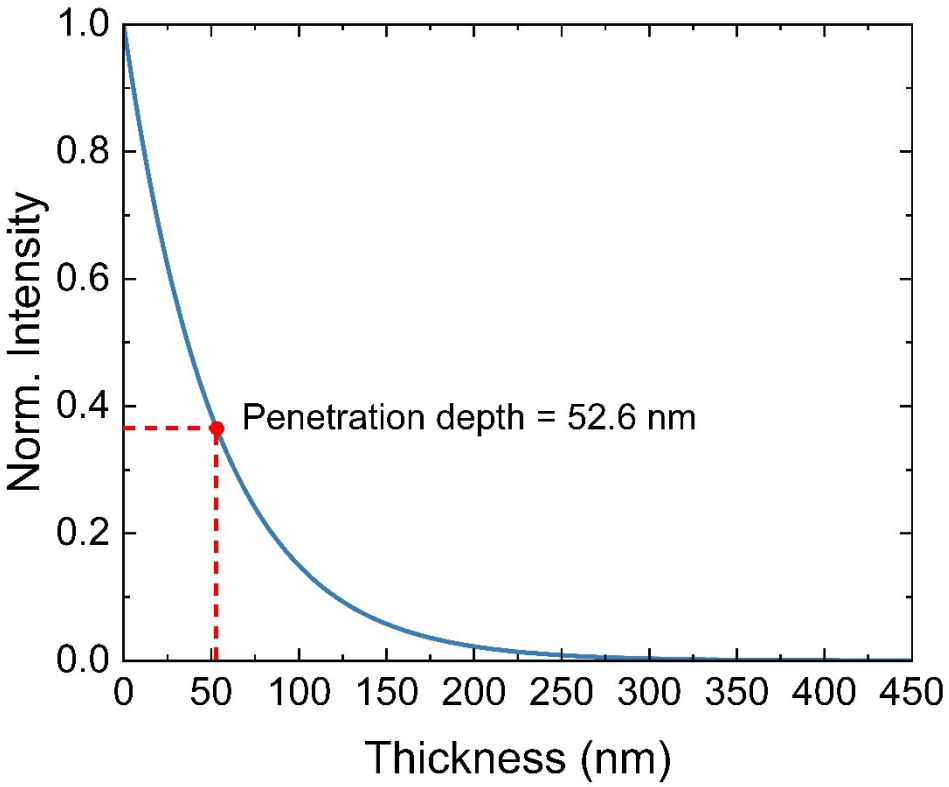

Figure S17. Normalized Beer-Lambert profile of the perovskite layer under the 400 nm excitation with a 1/e penetration depth of 52.6 nm.

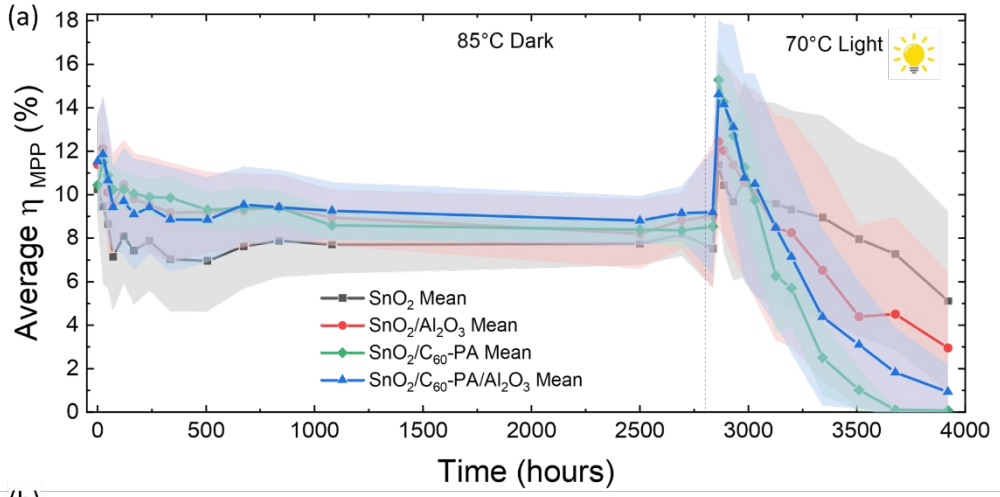
(a)
85°C Dark
70°C Light
Average η MPP (%)
Time (hours)
SnO2 Mean
SnO2/Al2O3 Mean
SnO2/C60-PA Mean
SnO2/C60-PA/Al2O3 Mean

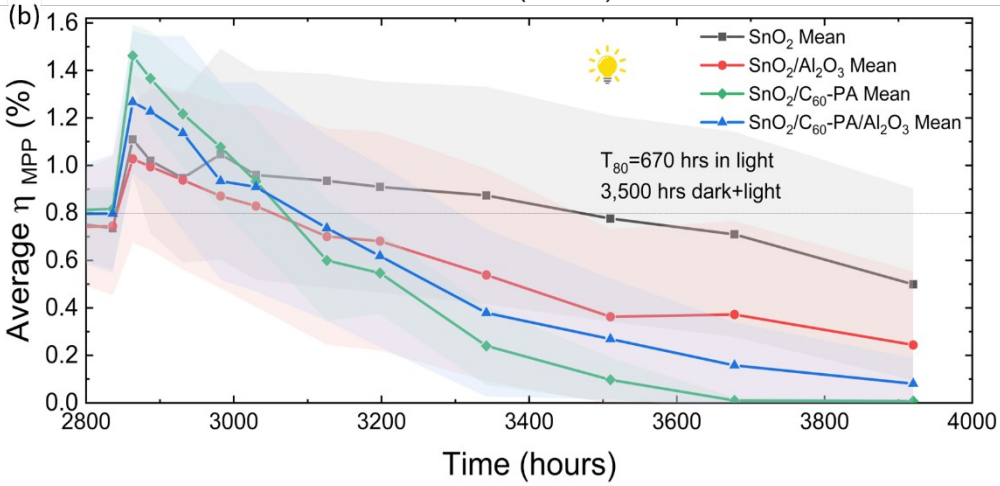
(b)
Average η MPP (%)
Time (hours)
SnO2 Mean
SnO2/Al2O3 Mean
SnO2/C60-PA Mean
SnO2/C60-PA/Al2O3 Mean
T80=670 hrs in light
3,500 hrs dark+light

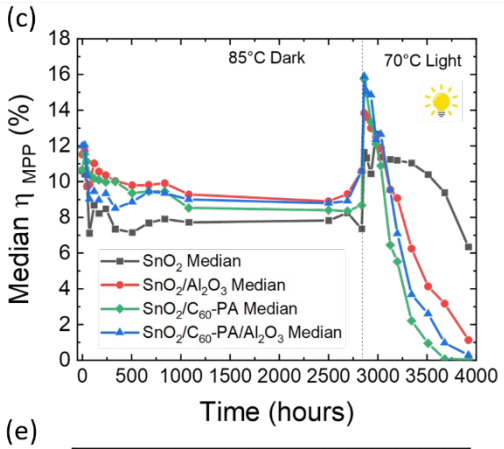
(c)
85°C Dark
70°C Light
Median η MPP (%)
Time (hours)
SnO2 Median
SnO2/Al2O3 Median
SnO2/C60-PA Median
SnO2/C60-PA/Al2O3 Median

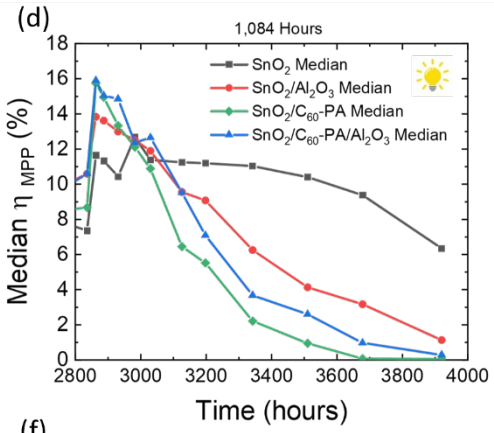
(d)
1,084 Hours
Median η MPP (%)
Time (hours)
SnO2 Median
SnO2/Al2O3 Median
SnO2/C60-PA Median
SnO2/C60-PA/Al2O3 Median

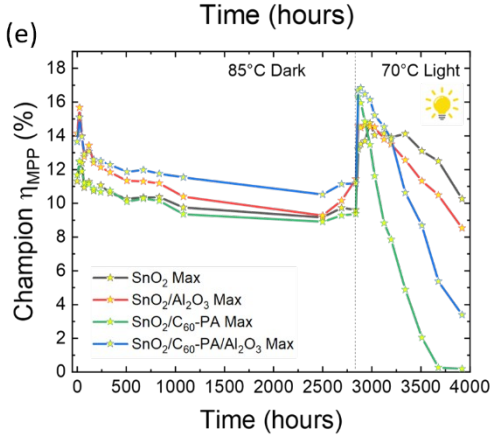
(e)
85°C Dark
70°C Light
Champion ηMPP (%)
Time (hours)
SnO2 Max
SnO2/Al2O3 Max
SnO2/C60-PA Max
SnO2/C60-PA/Al2O3 Max

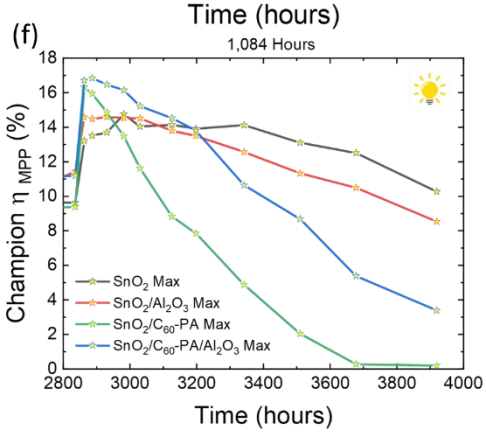
(f)
1,084 Hours
Champion η MPP (%)
Time (hours)
SnO2 Max
SnO2/Al2O3 Max
SnO2/C60-PA Max
SnO2/C60-PA/Al2O3 Max

Figure S18. (a) Average η_{MPP} of devices with different ETL modification, first aged under an 85° C dark, nitrogen environment for 2,800 h and then taken into 70±5 °C AM 1.5G for 1,084 hours. (b) Average η_{MPP} of devices normalized by the initial efficiency and zoomed into the last 1,084 h under the light. The colored areas denote their standard deviation. (c) Median η_{MPP} of these devices. (d) Median η_{MPP} of devices zoomed into the last 1,084 hrs under the light. (e) Champion device η_{MPP} for each condition. (f) Champion device η_{MPP} zoomed into the last 1,084 h under the light.

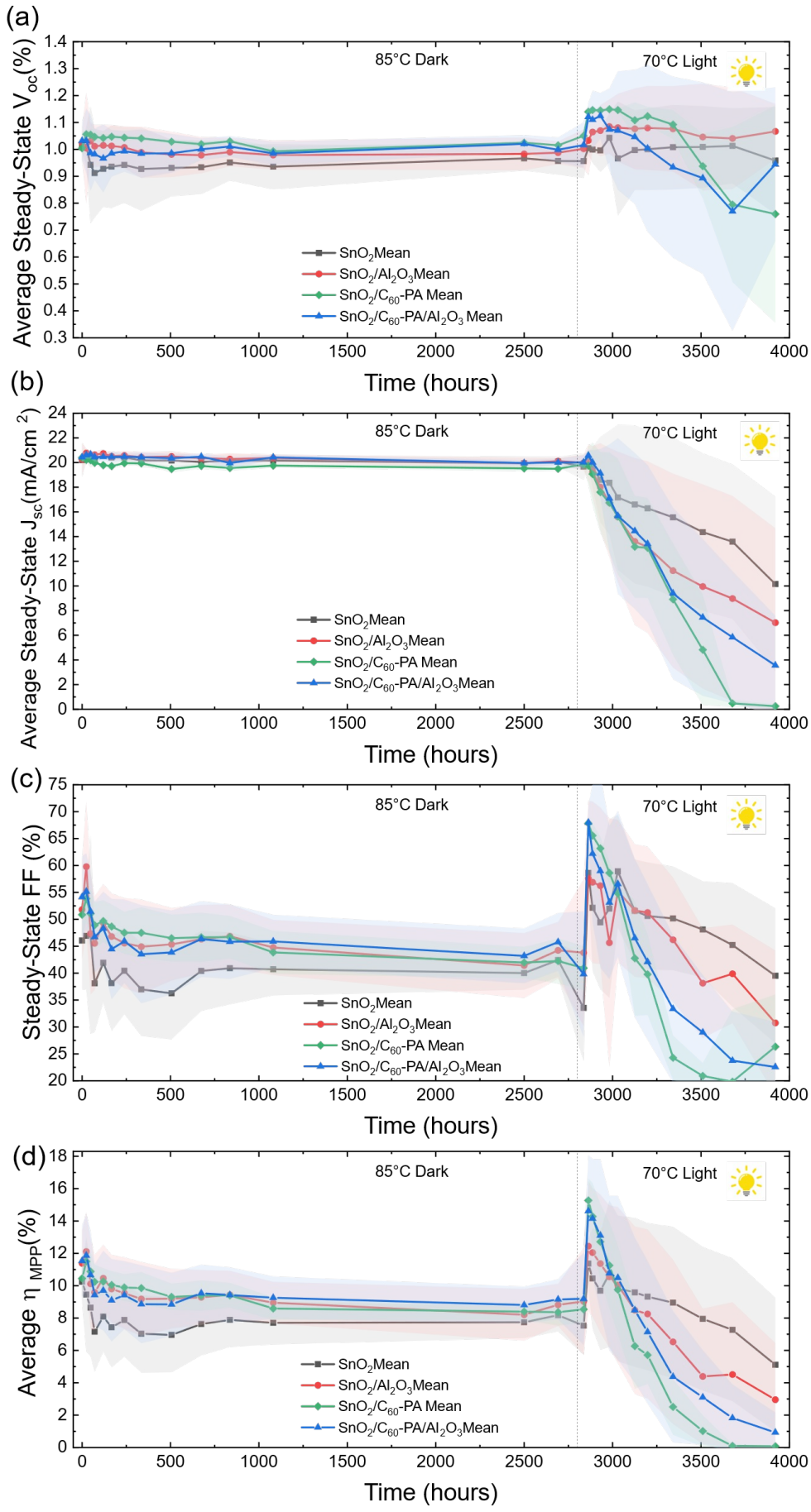
(a)
Average Steady-State V_{oc}(%)
85°C Dark
70°C Light
SnO_2Mean
SnO_2/Al_2O_3Mean
SnO_2/C_{60}-PA Mean
SnO_2/C_{60}-PA/Al_2O_3 Mean
Time (hours)
(b)
Average Steady-State J_{sc}(mA/cm^2)
85°C Dark
70°C Light
SnO_2Mean
SnO_2/Al_2O_3Mean
SnO_2/C_{60}-PA Mean
SnO_2/C_{60}-PA/Al_2O_3Mean
Time (hours)
(c)
Steady-State FF (%)
85°C Dark
70°C Light
SnO_2Mean
SnO_2/Al_2O_3Mean
SnO_2/C_{60}-PA Mean
SnO_2/C_{60}-PA/Al_2O_3Mean
Time (hours)
(d)
Average η_{MPP}(%)
85°C Dark
70°C Light
SnO_2Mean
SnO_2/Al_2O_3Mean
SnO_2/C_{60}-PA Mean
SnO_2/C_{60}-PA/Al_2O_3Mean
Time (hours)

Figure S19. Evolution of n-i-p device parameters (same devices as in **Figure S18**). Devices were first aged under an 85° C dark, nitrogen environment for 2,800 h and then taken into 70±5 °C AM 1.5G for 1,084 hours. (a) Average steady-state V_{oc}. (b) Average steady-state J_{sc}. (c) Average steady-state *FF*. (d) Average η_{MPP} of devices. The colored areas denote their standard deviation.

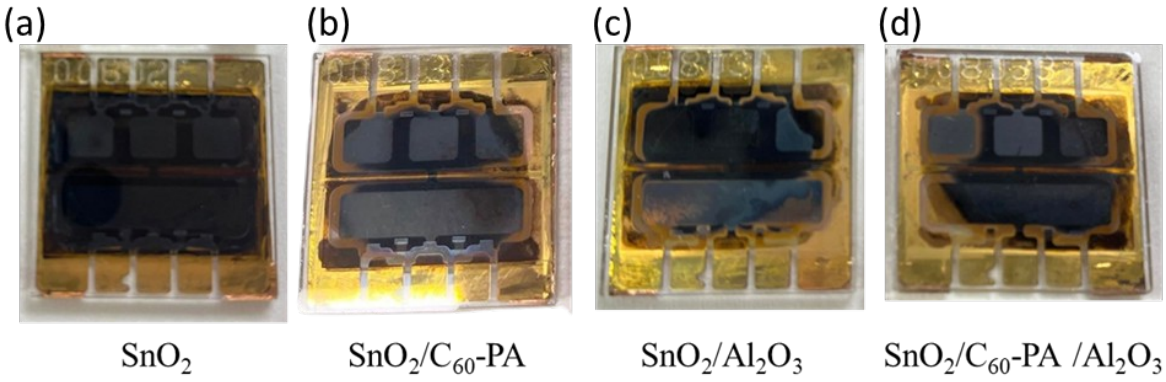

Figure S20. Devices with C_{60}-PA and Al_2O_3 modifications at the end of the aging test presented in Fig S18, seen from the glass side.

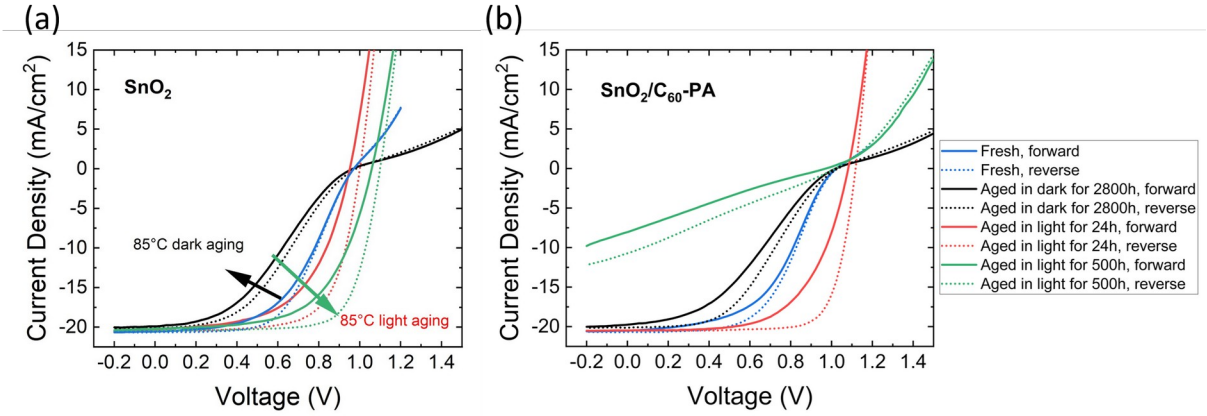

Figure S21. (a) J-V curve evolution of SnO_2 devices first aged under 85°C dark and then 70°C light. (b) J-V curve evolution of SnO_2/C_{60}-PA devices first aged under 85°C dark and then 70°C light.

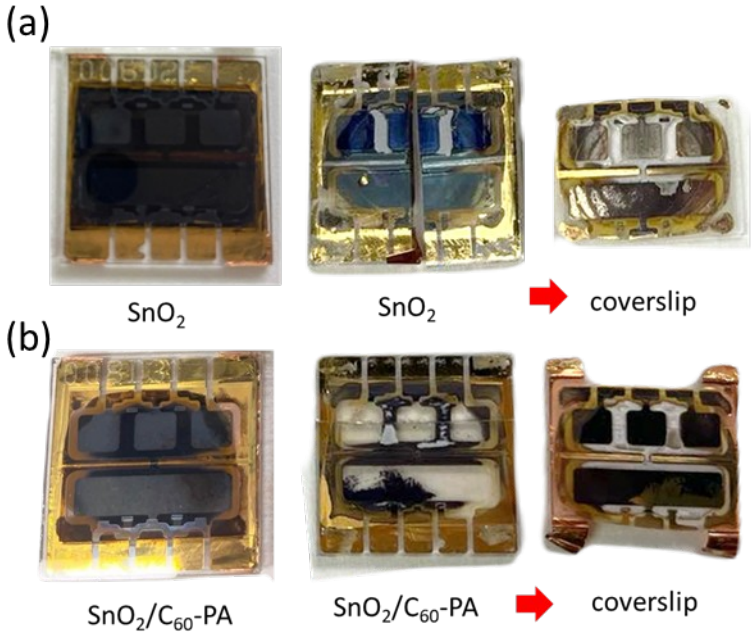

Figure S22. Photographs of solar cells at the end of the 3,900-h thermal and light aging test (left) and the substrate and coverslip after cleaving and cracking (right) (a) SnO_2 based-devices (b) SnO_2/C_{60}-PA based-devices.

References

(1) Hau, S. K.; Cheng, Y.-J.; Yip, H.-L.; Zhang, Y.; Ma, H.; Jen, A. K.-Y. Effect of Chemical Modification of Fullerene-Based Self-Assembled Monolayers on the Performance of Inverted Polymer Solar Cells. *ACS Appl. Mater. Interfaces* **2010**, *2* (7), 1892–1902. https://doi.org/10.1021/am100238e.

(2) Habisreutinger, S. N.; Wenger, B.; Snaith, H. J.; Nicholas, R. J. Dopant-Free Planar n–i–p Perovskite Solar Cells with Steady-State Efficiencies Exceeding 18%. *ACS Energy Lett.* **2017**, *2* (3), 622–628. https://doi.org/10.1021/acsenergylett.7b00028

(3) de Mello, J. C.; Wittmann, H. F.; Friend, R. H. An Improved Experimental Determination of External Photoluminescence Quantum Efficiency. *Adv. Mater.* **1997**, *9* (3), 230–232. https://doi.org/10.1002/adma.19970090308.

(4) Kirchartz, T.; Márquez, J. A.; Stolterfoht, M.; Unold, T. Photoluminescence-Based Characterization of Halide Perovskites for Photovoltaics. *Adv. Energy Mater.* **2020**, *10* (26), 1904134. https://doi.org/10.1002/AENM.201904134.

(5) Tiwana, P.; Parkinson, P.; Johnston, M. B.; Snaith, H. J.; Herz, L. M. Ultrafast Terahertz Conductivity Dynamics in Mesoporous TiO_2: Influence of Dye Sensitization and Surface Treatment in Solid-State Dye-Sensitized Solar Cells. *J. Phys. Chem. C*

2010, *114* (2), 1365–1371. https://doi.org/10.1021/jp908760r.

(6) Wehrenfennig, C.; Liu, M.; Snaith, H. J.; Johnston, M. B.; Herz, L. M. Charge-Carrier Dynamics in Vapour-Deposited Films of the Organolead Halide Perovskite $CH_3NH_3PbI_{3-x}Cl_x$. *Energy Environ. Sci.* **2014**, *7* (7), 2269–2275. https://doi.org/10.1039/C4EE01358A.

(7) Xia, C. Q.; Peng, J.; Poncé, S.; Patel, J. B.; Wright, A. D.; Crothers, T. W.; Uller Rothmann, M.; Borchert, J.; Milot, R. L.; Kraus, H.; Lin, Q.; Giustino, F.; Herz, L. M.; Johnston, M. B. Limits to Electrical Mobility in Lead-Halide Perovskite Semiconductors. *J. Phys. Chem. Lett.* **2021**, *12* (14), 3607–3617. https://doi.org/10.1021/acs.jpclett.1c00619.

(8) Beard, M. C.; Turner, G. M.; Schmuttenmaer, C. A. Transient Photoconductivity in GaAs as Measured by Time-Resolved Terahertz Spectroscopy. *Phys. Rev. B* **2000**, *62* (23), 15764–15777. https://doi.org/10.1103/PhysRevB.62.15764.

(9) Miyata, A.; Mitioglu, A.; Plochocka, P.; Portugall, O.; Wang, J. T.-W.; Stranks, S. D.; Snaith, H. J.; Nicholas, R. J. Direct Measurement of the Exciton Binding Energy and Effective Masses for Charge Carriers in Organic–Inorganic Tri-Halide Perovskites. *Nat. Phys.* **2015**, *11* (7), 582–587. https://doi.org/10.1038/nphys3357.

(10) Motti, S. G.; Kober-Czerny, M.; Righetto, M.; Holzhey, P.; Smith, J.; Kraus, H.; Snaith, H. J.; Johnston, M. B.; Herz, L. M. Exciton Formation Dynamics and Band-Like Free Charge-Carrier Transport in 2D Metal Halide Perovskite Semiconductors. *Adv. Funct. Mater.* **2023**, *33* (32), 2300363. https://doi.org/https://doi.org/10.1002/adfm.202300363.

(11) Dittrich, T.; Bönisch, S.; Zabel, P.; Dube, S. High Precision Differential Measurement of Surface Photovoltage Transients on Ultrathin CdS Layers. *Rev. Sci. Instrum.* **2008**, *79* (11), 113903. https://doi.org/10.1063/1.3020757.

(12) Levine, I.; Al-Ashouri, A.; Musiienko, A.; Hempel, H.; Magomedov, A.; Drevilkauskaite, A.; Getautis, V.; Menzel, D.; Hinrichs, K.; Unold, T.; Albrecht, S.; Dittrich, T. Charge Transfer Rates and Electron Trapping at Buried Interfaces of Perovskite Solar Cells. *Joule* **2021**, *5* (11), 2915–2933. https://doi.org/10.1016/j.joule.2021.07.016.

(13) Henke, B. L.; Gullikson, E. M.; Davis, J. C. X-Ray Interactions: Photoabsorption, Scattering, Transmission, and Reflection at E = 50-30,000 eV, Z = 1-92. *At. Data Nucl. Data Tables* **1993**, *54* (2), 181–342. https://doi.org/https://doi.org/10.1006/adnd.1993.1013.

(14) Giannozzi, P.; Baroni, S.; Bonini, N.; Calandra, M.; Car, R.; Cavazzoni, C.; Ceresoli, D.; Chiarotti, G. L.; Cococcioni, M.; Dabo, I.; Dal Corso, A.; de Gironcoli, S.; Fabris, S.; Fratesi, G.; Gebauer, R.; Gerstmann, U.; Gougoussis, C.; Kokalj, A.; Lazzeri, M.; Martin-Samos, L.; Marzari, N.; Mauri, F.; Mazzarello, R.; Paolini, S.; Pasquarello, A.; Paulatto, L.; Sbraccia, C.; Scandolo, S.; Sclauzero, G.; Seitsonen, A. P.; Smogunov, A.; Umari, P.; Wentzcovitch, R. M. QUANTUM ESPRESSO: A Modular and Open-Source Software Project for Quantum Simulations of Materials. *J. Phys. Condens. Matter* **2009**, *21* (39), 395502. https://doi.org/10.1088/0953-8984/21/39/395502.

(15) Giannozzi, P.; Andreussi, O.; Brumme, T.; Bunau, O.; Buongiorno Nardelli, M.; Calandra, M.; Car, R.; Cavazzoni, C.; Ceresoli, D.; Cococcioni, M.; Colonna, N.;

Carnimeo, I.; Dal Corso, A.; de Gironcoli, S.; Delugas, P.; DiStasio, R. A.; Ferretti, A.; Floris, A.; Fratesi, G.; Fugallo, G.; Gebauer, R.; Gerstmann, U.; Giustino, F.; Gorni, T.; Jia, J.; Kawamura, M.; Ko, H.-Y.; Kokalj, A.; Küçükbenli, E.; Lazzeri, M.; Marsili, M.; Marzari, N.; Mauri, F.; Nguyen, N. L.; Nguyen, H.-V.; Otero-de-la-Roza, A.; Paulatto, L.; Poncé, S.; Rocca, D.; Sabatini, R.; Santra, B.; Schlipf, M.; Seitsonen, A. P.; Smogunov, A.; Timrov, I.; Thonhauser, T.; Umari, P.; Vast, N.; Wu, X.; Baroni, S. Advanced Capabilities for Materials Modelling with Quantum ESPRESSO. *J. Phys. Condens. Matter* **2017**, *29* (46), 465901. https://doi.org/10.1088/1361-648X/aa8f79.

(16) Ernzerhof, M.; Scuseria, G. E. Assessment of the Perdew–Burke–Ernzerhof Exchange-Correlation Functional. *J. Chem. Phys.* **1999**, *110* (11), 5029–5036. https://doi.org/10.1063/1.478401.

(17) Grimme, S.; Antony, J.; Ehrlich, S.; Krieg, H. A Consistent and Accurate Ab Initio Parametrization of Density Functional Dispersion Correction (DFT-D) for the 94 Elements H-Pu. *J. Chem. Phys.* **2010**, *132* (15), 154104. https://doi.org/10.1063/1.3382344.

(18) van Setten, M. J.; Giantomassi, M.; Bousquet, E.; Verstraete, M. J.; Hamann, D. R.; Gonze, X.; Rignanese, G.-M. The PseudoDojo: Training and Grading a 85 Element Optimized Norm-Conserving Pseudopotential Table. *Comput. Phys. Commun.* **2018**, *226*, 39–54. https://doi.org/https://doi.org/10.1016/j.cpc.2018.01.012.

(19) Adamo, C.; Barone, V. Toward Reliable Density Functional Methods without Adjustable Parameters: The PBE0 Model. *J. Chem. Phys.* **1999**, *110* (13), 6158–6170. https://doi.org/10.1063/1.478522.

(20) Song, J.; Zheng, E.; Bian, J.; Wang, X.-F.; Tian, W.; Sanehira, Y.; Miyasaka, T. Low-Temperature SnO_2-Based Electron Selective Contact for Efficient and Stable Perovskite Solar Cells. *J. Mater. Chem. A* **2015**, *3* (20), 10837–10844. https://doi.org/10.1039/C5TA01207D.

(21) Orlandi, G.; Negri, F. Electronic States and Transitions in C_{60} and C_{70} Fullerenes. *Photochem. Photobiol. Sci.* **2002**, *1* (5), 289–308. https://doi.org/10.1039/B200178K.

(22) Wang, H.; He, Y.; Li, Y.; Su, H. Photophysical and Electronic Properties of Five PCBM-like C_{60} Derivatives: Spectral and Quantum Chemical View. *J. Phys. Chem. A* **2012**, *116* (1), 255–262. https://doi.org/10.1021/jp208520v.

(23) Lu, X.; Akasaka, T.; Slanina, Z. *Handbook of Fullerene Science and Technology* ; Springer: Singapore, 2022. https://doi.org/10.1007/978-981-16-8994-9.

(24) Saraswati, T. E.; Setiawan, U. H.; Ihsan, M. R.; Isnaeni, I.; Herbani, Y. The Study of the Optical Properties of C_{60} Fullerene in Different Organic Solvents. **2019**, *17* (1), 1198–1212. https://doi.org/doi:10.1515/chem-2019-0117.

(25) Prades, J. D.; Cirera, A.; Morante, J. R.; Pruneda, J. M.; Ordejón, P. Ab Initio Study of NO_x Compounds Adsorption on SnO_2 Surface. *Sensors Actuators B Chem.* **2007**, *126* (1), 62–67. https://doi.org/https://doi.org/10.1016/j.snb.2006.10.040.

(26) Doubi, Y.; Hartiti, B.; Batan, A.; Siadat, M.; Labrim, H.; Tahiri, M.; Kotbi, A.; Thevenin, P.; Jouiad, M. Controlled SnO_2 Nanostructures for Enhanced Sensing of Hydrogen Sulfide and Nitrogen Dioxide. *Sensors Actuators B Chem.* **2025**, *440*, 137878. https://doi.org/https://doi.org/10.1016/j.snb.2025.137878.

(27) Ruhland, B.; Becker, T.; Müller, G. Gas-Kinetic Interactions of Nitrous Oxides with SnO_2 Surfaces. *Sensors Actuators B Chem.* **1998**, *50* (1), 85–94. https://doi.org/https://doi.org/10.1016/S0925-4005(98)00160-9.

(28) Xu, G.; Zhang, L.; He, C.; Ma, D.; Lu, Z. Adsorption and Oxidation of NO on Various SnO_2(110) Surfaces: A Density Functional Theory Study. *Sensors Actuators B Chem.* **2015**, *221*, 717–722. https://doi.org/https://doi.org/10.1016/j.snb.2015.06.143.

(29) Maiti, A.; Rodriguez, J. A.; Law, M.; Kung, P.; McKinney, J. R.; Yang, P. SnO_2 Nanoribbons as NO_2 Sensors: Insights from First Principles Calculations. *Nano Lett.* **2003**, *3* (8), 1025–1028. https://doi.org/10.1021/nl034235v.

(30) Clark, T.; Chandrasekhar, J.; Spitznagel, G. W.; Schleyer, P. V. R. Efficient Diffuse Function-Augmented Basis Sets for Anion Calculations. III. The 3-21+G Basis Set for First-Row Elements, Li–F. *J. Comput. Chem.* **1983**, *4* (3), 294–301. https://doi.org/https://doi.org/10.1002/jcc.540040303.

(31) Krishnan, R.; Binkley, J. S.; Seeger, R.; Pople, J. A. Self-consistent Molecular Orbital Methods. XX. A Basis Set for Correlated Wave Functions. *J. Chem. Phys.* **1980**, *72* (1), 650–654. https://doi.org/10.1063/1.438955.

(32) Wang, J.; Fu, W.; Jariwala, S.; Sinha, I.; Jen, A. K.-Y.; Ginger, D. S. Reducing Surface Recombination Velocities at the Electrical Contacts Will Improve Perovskite Photovoltaics. *ACS Energy Lett.* **2019**, *4* (1), 222–227. https://doi.org/10.1021/acsenergylett.8b02058.

(33) Jariwala, S.; Burke, S.; Dunfield, S.; Shallcross, R. C.; Taddei, M.; Wang, J.; Eperon, G. E.; Armstrong, N. R.; Berry, J. J.; Ginger, D. S. Reducing Surface Recombination Velocity of Methylammonium-Free Mixed-Cation Mixed-Halide Perovskites via Surface Passivation. *Chem. Mater.* **2021**, *33* (13), 5035–5044. https://doi.org/10.1021/acs.chemmater.1c00848.

(34) de Quilettes, D. W.; Vorpahl, S. M.; Stranks, S. D.; Nagaoka, H.; Eperon, G. E.; Ziffer, M. E.; Snaith, H. J.; Ginger, D. S. Impact of Microstructure on Local Carrier Lifetime in Perovskite Solar Cells. *Science (80-.).* **2015**, *348* (6235), 683–686. https://doi.org/10.1126/science.aaa5333.

(35) Lindsey, C. P.; Patterson, G. D. Detailed Comparison of the Williams–Watts and Cole–Davidson Functions. *J. Chem. Phys.* **2008**, *73* (7), 3348–3357. https://doi.org/10.1063/1.440530.

(36) Taddei, M.; Jariwala, S.; Westbrook, R. J. E.; Gallagher, S.; Weaver, A. C.; Pothoof, J.; Ziffer, M. E.; Snaith, H. J.; Ginger, D. S. Interpreting Halide Perovskite Semiconductor Photoluminescence Kinetics. *ACS Energy Lett.* **2024**, *9* (6), 2508–2516. https://doi.org/10.1021/acsenergylett.4c00614.

(37) Stranks, S. D.; Eperon, G. E.; Grancini, G.; Menelaou, C.; Alcocer, M. J. P.; Leijtens, T.; Herz, L. M.; Petrozza, A.; Snaith, H. J. Electron-Hole Diffusion Lengths Exceeding 1 Micrometer in an Organometal Trihalide Perovskite Absorber. *Science (80-.).* **2013**, *342* (6156), 341–344. https://www.science.org/doi/10.1126/science.1243982

(38) Bonilla, R. S. Modelling of Kelvin Probe Surface Voltage and Photovoltage in Dielectric-Semiconductor Interfaces. *Mater. Res. Express* **2022**, *9* (8), 85901. https://doi.org/10.1088/2053-1591/ac84c8.

(39) Wojciechowski, K.; Stranks, S. D.; Abate, A.; Sadoughi, G.; Sadhanala, A.; Kopidakis, N.; Rumbles, G.; Li, C.-Z.; Friend, R. H.; Jen, A. K.-Y.; Snaith, H. J. Heterojunction Modification for Highly Efficient Organic–Inorganic Perovskite Solar Cells. *ACS Nano* **2014**, *8* (12), 12701–12709. https://doi.org/10.1021/nn505723h.

(40) Abrusci, A.; Stranks, S. D.; Docampo, P.; Yip, H.-L.; Jen, A. K.-Y.; Snaith, H. J. High-Performance Perovskite-Polymer Hybrid Solar Cells via Electronic Coupling with Fullerene Monolayers. *Nano Lett.* **2013**, *13* (7), 3124–3128. https://doi.org/10.1021/nl401044q.

(41) Liu, K.; Chen, S.; Wu, J.; Zhang, H.; Qin, M.; Lu, X.; Tu, Y.; Meng, Q.; Zhan, X. Fullerene Derivative Anchored SnO_2 for High-Performance Perovskite Solar Cells. *Energy Environ. Sci.* **2018**, *11* (12), 3463–3471. https://doi.org/10.1039/C8EE02172D.

(42) Warby, J.; Zu, F.; Zeiske, S.; Gutierrez-Partida, E.; Frohloff, L.; Kahmann, S.; Frohna, K.; Mosconi, E.; Radicchi, E.; Lang, F.; Shah, S.; Peña-Camargo, F.; Hempel, H.; Unold, T.; Koch, N.; Armin, A.; De Angelis, F.; Stranks, S. D.; Neher, D.; Stolterfoht, M. Understanding Performance Limiting Interfacial Recombination in Pin Perovskite Solar Cells. *Adv. Energy Mater.* **2022**, *12* (12), 2103567. https://doi.org/https://doi.org/10.1002/aenm.202103567.